Genesis: The Search for Origins

The Curation and Contamination Control of Returned Solar Wind Samples

by

Benjamin K. Jackson

M.Eng. Aerospace Materials Engineering
Imperial College London, UK 2003

SUBMITTED TO THE DEPARTMENT OF MATERIALS SCIENCE AND ENGINEERING IN PARTIAL FULFILMENT OF THE REQUIREMENTS FOR THE DEGREE OF

MASTER OF SCIENCE IN MATERIALS SCIENCE AND ENGINEERING
AT THE
MASSACHUSETTS INSTITUTE OF TECHNOLOGY

SEPTEMBER 2005

Signature of the Author: _____
Department of Materials Science and Engineering
June 30th 2005

Certified by: _____
Samuel M. Allen
POSCO Professor of Physical Metallurgy
Thesis Supervisor

Accepted by: _____
Gerbrand Ceder
R. P. Simmons Professor of Materials Science and Engineering
Chairman, Departmental Committee of Graduate Students

Genesis: The Search for Origins

The Curation and Contamination Control of

Returned Solar Wind Samples

by

Benjamin K. Jackson

Submitted to the Department of Materials Science and Engineering
On September, 2005 in Partial Fulfilment of the
Requirements for the Degree of Master of Science in
Materials Science and Engineering

ABSTRACT

The purpose of the studies carried out in this thesis was to aid in the curation of samples of solar wind returned to earth on the Genesis spacecraft.

An experimental study was carried out to aid development of a set of protocols for the laser scribing and subdivision of the Genesis silicon collector array materials. Optimisation of the scribing speed and the positioning of the focal point of the laser were carried out. It was found that scribe width was independent of both factors. Slower scribing speeds were found to produce deeper scribes, while heating effects were minimised with faster speeds. Vertical movement of the stage of 5 μm/pass was found to optimise the focal point of the laser, and minimise heating effects. A procedure to measure the flexural modulus of samples was proposed to quantify the success of the optimisation of the scribing parameters.

A theoretical study was carried out to develop a predictive kinetic model for the oxidation of the silicon collector arrays during flight. The mechanism proposed for the increase in oxide thickness over that present pre-flight was the formation of a less-dense suboxide at the SiO_2/Si interface. The driving force is the elevated temperature of the collectors during collection, in the vacuum of space. A kinetic model was developed and growth rate expressions derived for two limiting kinetic cases. It was not possible to apply these expressions to the Genesis sample conditions, as the measurement of several experimental parameters was beyond the time limits of this study. A second model was developed alongside literature models to reduce further the number of unknown variables. Finally, the maximum possible thickness of oxide that could grow on the silicon surface was calculated. This was found to be 25 Å, representing a 47 % increase over the original 17Å of SiO_2 present pre-flight. It was noted that there was a non-linear increase of total oxide thickness with increase in suboxide thickness to due to density differences between Si and SiO, and SiO_2 and SiO.

Thesis Supervisor: Samuel M. Allen

Title: POSCO Professor of Physical Metallurgy

Table of Contents

List of Illustrations

List of Illustrations

4.0 Kinetic Modelling of SiO_2 Band Broadening

5.0 Summary and Conclusions

There are no figures present in this section

6.0 Bibliography

There are no figures present in this section

List of Tables

Acknowledgements

Firstly I would like to thank my advisor, Professor Sam Allen, for his guidance, patience and kind words when things hit the ground quickly, or otherwise went awry and for enduring the countless lengthy long distance phone calls.

Next thanks goes to Dr. Howard "Vern" Lauer for being an invaluable source of encouragement and knowledge and for being a pleasure to work with during my time at the Lyndon B. Johnson Space Center.

I would also like to thank Georg-Anne Robinson and Suzanne Summers for 'showing me the ropes' around Building 31 and for listening to me complain.

I would like to thank my office mates Dr.'s Mark Matney, Tim Cleghorn, and Edwin Barker for their thesis advice, being my human spelling and grammar checkers, and for making me laugh every day.

Last, but not least, I would like to thank my girlfriend Heather Fireman for her kindness and support and for putting up with me over the last few months.

Financial support via National Aeronautics and Space Administration Awards #NNJ05HB37G gratefully acknowledged.

Thanks goes to Prof. Karen McNamara for making the opportunity to work on this project possible.

For those I worked with and knew at JSC and MIT who were not mentioned here, let me say I appreciate everything that was done for me to make my paperwork, research and degree go as smoothly as possible, no matter what was thrown (or dropped) in its path.

1.0 Introduction

The Genesis spacecraft was launched on August 8th 2001 from the Kennedy Space Center, FL aboard a Boeing Delta II rocket, pictured in *Fig 1.1*. The Genesis spacecraft can be seen in its launch configuration in the faring of the rocket in *Fig 1.2*. The aim of the Genesis Mission was to collect atoms of solar wind and return them to Earth for analysis.

The Genesis mission goals were as follows [1]:

- To obtain precise measure of solar isotopic abundances. The Genesis spacecraft will measure isotopic compositions of oxygen, nitrogen, and noble gases. These data will enable scientists to better understand the isotopic variations in meteorites, comets, lunar samples, and planetary atmospheres.
- To obtain greatly improved measures of solar elemental abundances.
- To provide a reservoir of solar matter for 21st century science research, eliminating the need for future solar wind sample return missions.

Fig 1.1: Genesis Launch 8th August 2001 at KSC

The sun contains 99% of the matter in our solar system, and the solar wind (a collection of atoms, ions and other high-energy particles) represents a small fraction of that matter and is released into space in the form of high-velocity particle streams. The solar wind is composed of the very matter that formed the planets – the solar nebula. Analysis of the solar wind, it is hoped, will reveal the composition of the solar nebula and will improve understanding of evolutionary process by which the planets within our solar system evolved [1].

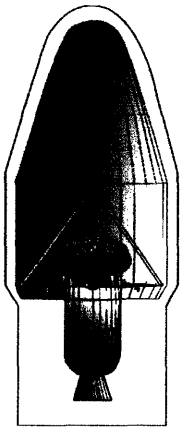

Fig 1.2: Launch Configuration

The Genesis probe was positioned at the LaGrange point 1, known as L1, between the Earth and the sun. This is a point outside of the earth's magnetic field, and at a point where the Earth's and sun's gravity are in balance. Thus while positioned at L1 Genesis will orbit the sun with the same angular velocity as the Earth orbits the sun. The probe remained at this point for a total collection period of 2.5 years. During the 2.5 years the probe collected solar wind by the process of ion implantation of solar wind particles on the surface of ultra-pure collector materials. The collector materials consisted of mainly Si, sapphire and Ge wafers of very high purity, ranging in thickness from 550 μm to 700 μm on three different deployable arrays. The high purity wafers allowed the detection of even trace amounts of implanted species present within the wafer. It was predicted that the solar wind species would lie within a narrow band, not more than 100 nm from the collector surface [2, 3].This study is limited only to the silicon collectors as they are the most numerous collectors within the arrays. Future work would be to apply the techniques developed in this study to the other collector materials. *Fig 1.3* shows the Genesis spacecraft with its collecting arrays deployed. There are several collection arrays, each responsible for collecting a different regime (speed) of solar wind: interstream, coronal hole, and coronal mass ejection. To distinguish these types in real time the spacecraft is

equipped with a Genesis Electron Monitor (GEM) and a Genesis Ion Monitor (GIM) [28]. It is only by comparison of the different regimes of solar wind and comparing them to the bulk collector (always exposed) that the composition of the solar wind may be determined. The GEM and GIM instruments deploy the appropriate array as a change in solar wind regime is detected. There is also a special collector called the *concentrator target*. This collector is designed to collect the most precious of the Genesis samples – isotopes of oxygen and nitrogen – two of the elements essential for life. The collector is surrounded by a 'mirror' that concentrates the solar wind onto the central target materials (silicon carbide and diamond on a gold support). This is hoped to significantly increase the yield of the returned oxygen and nitrogen species over that of the main collector arrays.

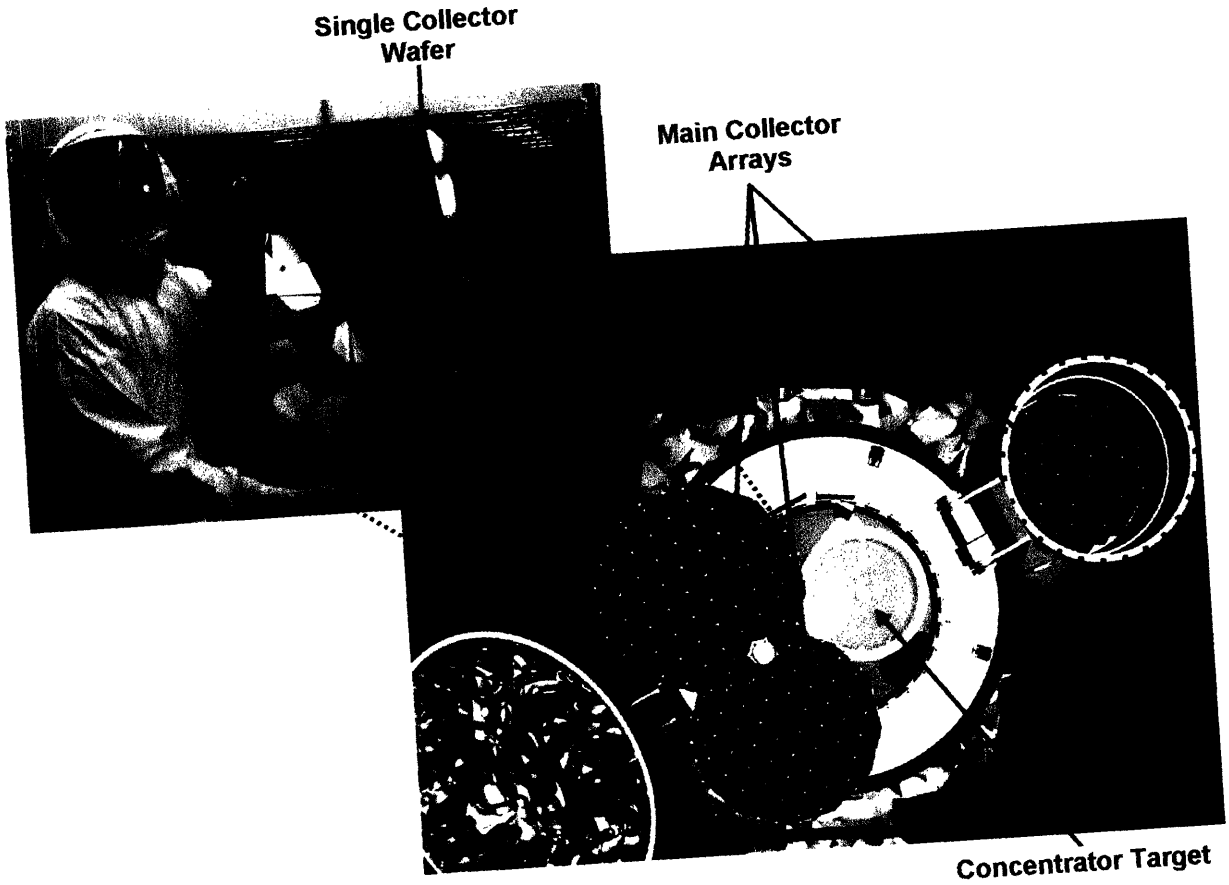

Fig 1.3: Genesis Probe in Collection Configuration

The Genesis Mission is the first sample return mission of extra-terrestrial material since the Apollo 17 mission in 1972 returned with the last set of lunar samples. Only about *0.4 mg* of material in total is expected to be recovered from the solar wind. It is therefore of the utmost importance to protect the collector materials from contamination from terrestrial sources. From assembly to sample distribution it was the aim of the mission to maintain the cleanliness of the array materials to a '*Class 10*' clean-room standard (less than 10 particles of dust per cubic foot).

In the interest of contamination control and in the interest of avoiding fracture of the brittle collectors, a unique recovery method was designed for the Genesis return capsule. The capsule was to re-enter the earth's atmosphere, and initially be slowed by a circular drogue parachute. After sufficient deceleration the drogue 'chute was to be jettisoned and a parafoil be deployed. This would cause the Genesis return capsule to slowly spiral towards the earth, allowing for a helicopter to capture it in mid-air and bring it safely to a clean-room environment. An illustration of this is shown in *Fig 1.4*. The reason behind such an elaborate capture procedure is that the traditional splash-down landing would introduce the possibility of water contamination, and also such a hard landing would be likely to shatter the collector arrays.

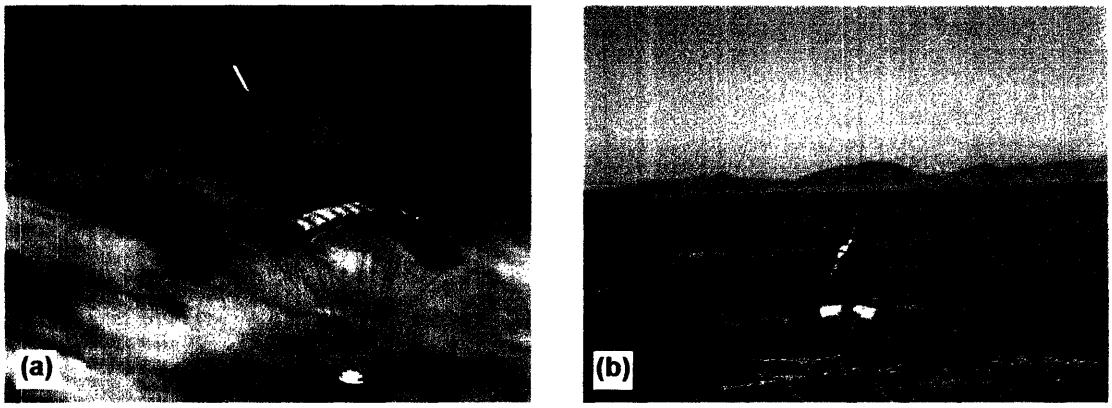

Fig 1.4: Mid-air capture of Genesis Sample Return Capsule: (a) Artists Rendering; (b) Practice Capture

Unfortunately, on September 8th 2004, Genesis crashed to the ground over Utah Test and Training Range (UTTR), after both parachutes failed to deploy. The canister containing the collector arrays was badly damaged, and the collector arrays were exposed to the atmosphere, and worse still the sand and mud of the Utah desert. Images of the crash are shown in *Fig 1.5*.

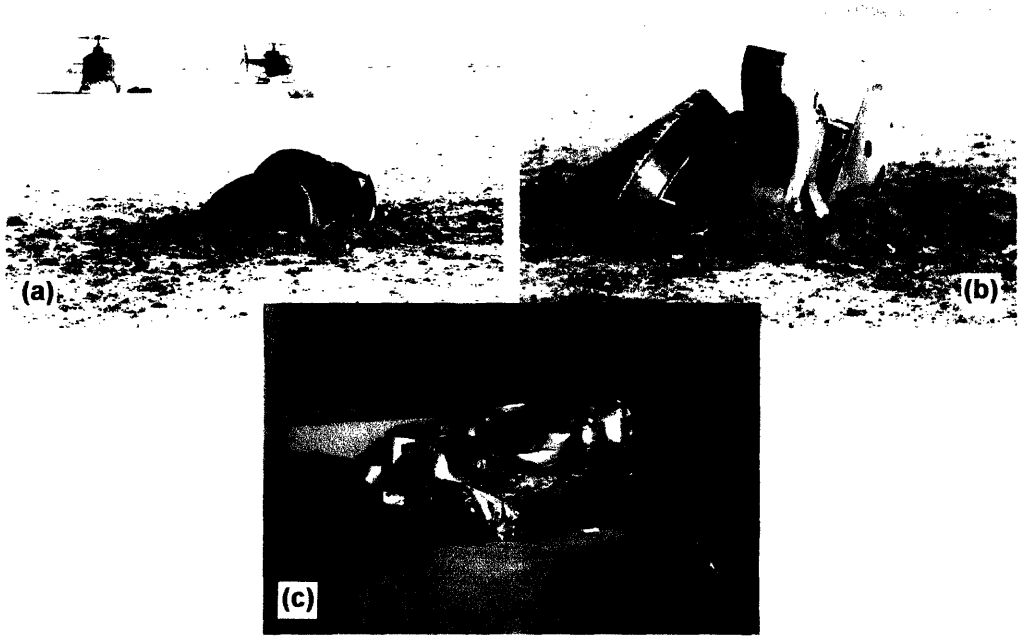

Fig 1.5: Wreckage of Genesis: (a) & (b) Genesis impact site; (c) Science Canister containing collector arrays removed from wreckage in clean room

[1] suggested that the most likely cause of the crash was an incorrectly mounted 'g-switch', pictured in *Fig 1.6*. During the assembly of the probe, the avionics box was mounted upside down, meaning the G-switch was unable to register the deceleration of the probe during re-entry, and therefore never triggered the explosive charges to deploy the parachutes, causing the capsule to impact the Utah desert at 87.6 m s^{-1} (196 mph).

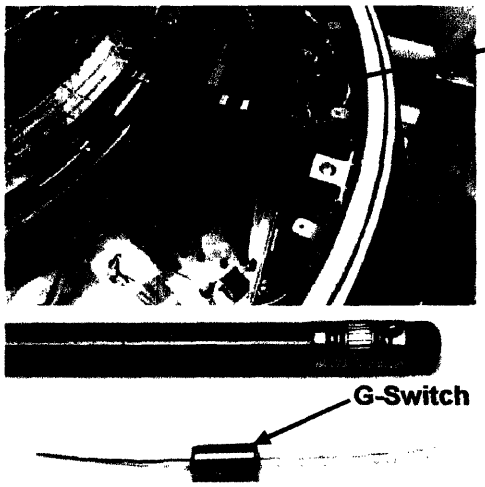

Fig 1.6: The cause of the Genesis crash – improperly oriented Avionics Equipment

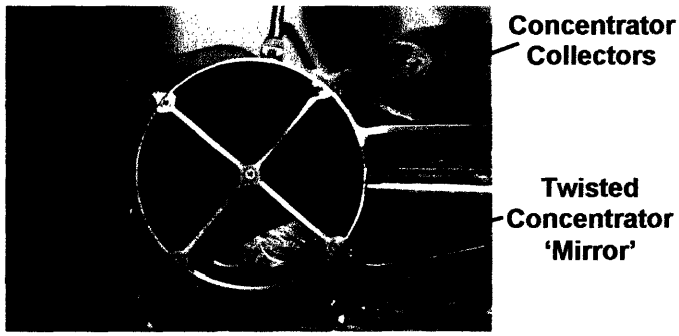

Fig 1.7: Recovered Concentrator Target

Since September 8th, extensive recovery efforts have been made, attempting to minimise the impact of the crash on the mission goals. At of the time of writing of this report, the extent of the collector damage is still being assessed. However, preliminary analyses suggest that solar material has indeed been recovered from some of the returned collectors. The precious concentrator target faired the best out of all of the instrumentation, with more than 75% of the collector area remaining intact, as shown in *Fig 1.7*.

The research presented in this thesis has been split into two areas:

1. *The clean subdivision of the collector materials once they were returned to Earth.* Prior to the crash it was of utmost importance to preserve the cleanliness of the collector arrays. It was also necessary in order to maximise the scientific return of the mission to distribute the collector materials to the scientific community. Research was performed to help develop protocols for the subdivision of the returned samples using a bench-top commercial laser scribing system so as to preserve as close as possible the Class 10 environment in which they were returned. Unfortunately this research area was reprioritised after the events of September 8th, limiting the results obtained from this part of the study.
2. *A kinetic model to characterize and predict the amount of oxidation on the collector arrays during their time in space.* A finite layer of oxide was present on the surface of the silicon collector prior to flight, and was unavoidable. This section of research investigates the extent to which the layer of silicon dioxide will broaden due to the elevated-temperature exposure of the collector materials to the sun.

The research performed by the author in this thesis represents but a very small part of the work of the Genesis team, and it is expected the Genesis project will continue for many years to come, possibly providing us with answers to some of the most elusive questions on evolution of the solar system to date.

2.0 Critical Review of Current Literature

2.1 Subdivision of Collector Materials

The development of a suitable set of protocols for the subdivision of the returned Genesis collector materials is a unique problem. The research performed at the Johnson Space Centre in the summer of 2003 does not have precedent, and was entirely experimental based on the goals set out in [1]. Very little literature on the subject could be located.

2.2 Development of a Kinetic Model for the Oxide Growth on Si Collectors

The growth of an oxide layer on the surface of silicon has been a subject of great interest for at least the last 30 years. This is due to the ever increasing demands placed on the performance and miniaturisation of logic and memory devices. The core technologies include metal-on-semiconductor (MOS), complimentary-metal-on-semiconductor (CMOS) devices [4], and highly integrated metal-oxide-semiconductor field effect-transistors (MOSFETs) [5]. In order to manufacture such devices that require very large scale (VLSI) and ultra-large scale (ULSI) integration, precise control of silicon oxide films must be achieved for film thicknesses ranging from 3 to 100 nm [6, 7]. Therefore there has been a great deal of research into the oxidation process, its associated kinetics, and the preparation of the silicon substrate during device manufacture [8-10].

The first important step in device manufacture is to remove the native oxide that grows at room temperature on bare single-crystal Si substrates. The existence of a native oxide prevents the precise control necessary on the thickness and quality of the very thin gate oxides [9]. The structure of the native oxide, which is composed of a homogenous mixture of silicon oxidation states (both SiO and SiO_2 exist), is that of irregular shaped islands of oxide of varying thickness across the surface of a silicon wafer [9, 10]. This oxide is typically stripped by chemically etching the surface of the silicon to leave a hydrogen-terminated silicon surface that will inhibit further native oxide formation. The required gate oxide thickness may then be accurately deposited on the substrate [8].

The pioneering research into the controlled thermal oxidation of the silicon surface was performed by Deal and Grove [11] in 1965. They employed what has since found to be an overly simplistic theory of the oxidation mechanism. The premise of their model was that oxidation rates were controlled by two factors: the oxidation reaction at the silicon/oxide interface, and the diffusion of the oxygen through the oxide layer, leading to a "linear-parabolic" oxide growth rate law. This model agreed well with most of the experimental data at the time, and is still the basis of some of the major oxidation simulation programs used in industry [12]. However, the major problem with the Deal-Grove model is that it fails to predict accurately the growth of oxide films below 20 nm [12, 6, 7], which is precisely the thicknesses of oxide that are in use in today's technology. These oxides are in what is termed the "anomalous regime" or "thin oxide regime", and their growth rates have been observed to be much higher than predicted by the Deal-Grove model. Since the 60's there have been many competing models developed that aim to better predict the oxide behaviour within the anomalous regime. Due to the extensive literature available, only a small selection of the more widely accepted alternative models to the Deal-Grove theory are presented here.

Han and Helms [13] proposed that oxide growth proceeds by two parallel rate-limiting processes involving molecular and atomic oxygen species. They modelled oxide growth by a diffusion rate-limiting step in parallel with a linear-parabolic growth rate similar to that of Deal-Grove. Their proposed law uses three experimentally determined fitting parameters, allowing a much closer fit to experimental data than was possible with Deal-Grove. Their model fits well data obtained in the anomalous oxidation regime. They clearly identify the existence of two different mechanisms in the oxidation process, suggesting that there may be an intermediate step/product formed before SiO_2.

Reisman et al. [14] also proposed a model that agreed well with experimental data in the thin regime. They proposed that the oxidation rate was controlled entirely by the interfacial reaction at the silicon/oxide interface and the subsequent viscous flow of the newly formed oxide to accommodate the volume expansion at the interface. As more oxide is formed the average viscosity of the film increases, thus reducing the oxidation rate with time. The model therefore predicts accelerated growth for very thin oxides, as is observed experimentally.

Kageshima et al. [5] propose a very different model. They suggest that the rate of oxide growth is governed by the rate of emission of Si atoms from the bulk Si at the interface, and their subsequent diffusion through the oxide layer. As a result of the oxidation reaction at the interface to form SiO_2 there is an accumulation of strain due to the volume expansion. Thus to relax the Si lattice Si atoms are released into the SiO_2. For thin films, the Si is able to be rapidly transported away from the interface into the SiO_2 network, where it is then 'absorbed' into the SiO_2 network. However for thick films the many emitted Si atoms may remain stagnant at the interface, and prevent the further release of Si atoms. This will, they propose, reduce the rate of the interfacial reaction. This model thus predicts a faster growth rate for thin films, and fits with experimental data in the thin regime, without the need for any empirical fitting parameters.

Finally, perhaps the most extensively tested model is that from Massoud et al. [4, 15-18]. Massoud derived from his numerous experiments an entirely empirical law for the oxidation of silicon. His basis for doing this was that no single model available to him accurately predicted growth under all of his experimental conditions. He performed oxidation experiments on silicon samples under a variety of doping densities, oxygen partial pressures, crystallographic orientation and temperatures using *in situ* ellipsometry. The details of these experiments cannot be discussed fully in this thesis, but the reader is referred to [4, 15-18] for a more in-depth review of Massoud et al.'s work. In summary, although his growth law is empirical, he suggests that the reason for the initial 'ballistic growth' of the oxide layer is that the initial oxygen molecule incident on the bare Si surface forms an intermediate layer of SiO, preventing further oxygen from reaching the Si surface. As more oxygen is delivered, the partial pressure of oxygen is thought to increase to the point where the formation of SiO_2 is favoured, and the whole surface rapidly converts to SiO_2, accounting for the initial rapid oxidation rate (Massoud termed this the 'ballistic growth' phase) that is experimentally observed.

It can be seen that there are many different explanations and models offered to explain the growth characteristics of oxide(s) layer(s) on the surface of silicon. They all claim to fit experimental data, but offer fairly different explanations for the oxidation mechanism. Most of them seem to agree that the oxidation process involves the formation of an intermediate reaction product that then gets converted to SiO_2, and that substrate orientation makes a difference to the structure of the resulting oxide. It must be noted that all of the above models were developed for the oxidation of silicon *in air.* At this present time there does not exist a model, nor any experimental data, for the oxidation of silicon in a *vacuum*, such as is the case for Genesis. However, the suggestions as to the nature of the intermediate oxidation compound are a little more consistent. There have been many studies dedicated simply to defining the morphology of the Si/SiO_2 interface when the oxide is thermally grown on the substrate. A brief review of a selection of these studies follows.

Ourmazd et al. [19] performed TEM observations on the Si/SiO_2 interface. They proposed that the transition from crystalline Si to amorphous SiO_2 occurs by the formation of an ordered crystalline transition layer about 5Å thick. The most likely structure of this ordered phase is that of *tridymite*, a stable, bulk form of SiO_2. However, there exists very little support for these observations in the literature.

Grunthaner et al. [20] employed X-ray photoelectron spectroscopy (*XPS*) to examine the localisation and crystallographic dependence of Si^{+1} (Si_2O), Si^{+2} (SiO), and Si^{+3} (Si_2O_3) oxidation states at the Si/SiO_2 interface for (100)- and (111)-oriented substrates with gate oxide quality thermal oxides. They were able to quantitatively show that the Si^{+1} and Si^{+2} states were localised within 6-10Å, and that the Si^{+3} state existed further away from the interface, and extended ~30Å into the bulk SiO_2. They were also able to demonstrate a strong crystallographic dependence on

the distribution of the Si^{+1} and Si^{+2} states, such that the relative abundance of the Si^{+2} species was far greater than Si^{+1} on (100)-oriented substrates, and Si^{+1} was far more abundant on (111)-oriented substrates. Himpsel et al. [21] showed similar results to [20] using '*core level spectroscopy*'. They proposed this method could more straightforwardly resolve the different Si oxidation states. It failed to be as quantitative as [20] in terms of the distribution of the oxidation states through the thickness of the oxide layer, but did agree with the relative abundances and crystallographic dependence of the oxidation states found in [20]. Hattori et al. [22] performed independent XPS research on the system, and produced similar results to [20] and [21], but again failed to quantify the distribution of the oxidation states through the oxide thickness.

While [20-22] suggest that a number of suboxide states exist in the Si/SiO_2 system, Raider [23] explicitly identifies SiO (Si^{+2}) as the intermediate substance for oxidation Si to SiO_2. He goes on to experimentally demonstrate that if the step that forms SiO is inhibited, no further SiO_2 may be formed. He also proposes that SiO can exist as a stable phase within the system, or be oxidised further to form SiO_2.

da Silva Jr. et al. [24-26] propose [25] that the oxidation of the Si substrate occurs by the rapid initial formation of a self-affine oxidation front to a depth of ~≤ 30 Å, which then retains its depth and moves into the Si bulk leaving fully oxidised SiO_2 behind it. The predictions of this model to are a good fit to experimental data, especially in the thin regime [26]. da Silva then goes on to develop a Monte Carlo simulation [24] to give further support to the model. The Monte Carlo simulation predicts parabolic growth of the oxidation front (i.e., during the thin regime), followed by a slower oxidation rate consistent with that predicted by Deal-Grove for thicker films.

To summarise, there exist many competing models for the oxidation mechanism of the Si/SiO_2 system based on the initial work by Deal and Grove [11], and there is no clear 'right answer' at this time. No model exists that specifically predicts oxide growth in a vacuum, as is the case for the Genesis collectors. However, there is good support for there being an intermediate oxidation state (most likely SiO on (100)-oriented Si); the intermediate phase is rapidly formed at the beginning of the oxidation process; the intermediate can form a thin stable layer (oxidation front) at the Si/oxide interface; the formation of the transition layer is essential to the further oxidation to SiO_2.

Most of the referenced studies have been concerned with the oxidation of silicon at relatively high temperatures (~800 → 1000°C). This is the temperature range of interest in industry, as it allows the growth of SiO_2 in a reasonable industrial timescale (on the order of minutes or hours, rather than days or months) for the mass production of electronic devices. The only studies that were found in the literature that concerned room temperature, or any temperature close to the ~165°C [2] to which the Genesis collectors would be exposed, are those that study the native oxide formation and associated kinetics [8-10], which are not entirely relevant to the required model for Genesis. Lewis et al. considered 'low temperature' to be 600°C during his series of experiments in the 'low temperature regime' [39]. The development of a kinetic model for the Genesis mission represents the first study to attempt to model the kinetics of very low temperature oxidation of silicon in a vacuum.

3.0 The Laser Scribing of Collector Materials

The aim this section of work was to develop a set of protocols for the subdivision of the Genesis collector array materials upon their return to Earth in September 2004. The majority of the work in this section was completed prior to the Genesis landing. However, due to extensive damage to the collector arrays during landing, the research into their subdivision was cut short. The work presented in this section summarises the results obtained prior to the September 8th landing accident.

Preliminary studies into scribing methodology suitable for the Genesis collector materials [2] have recommended the use of a laser scribing system to scribe the back side of the samples (only penetrating through a partial thickness). The depth of the cut was to be sufficiently large so as to allow easy cleavage along the scribed path without the need for a through thickness scribe (which would give undesirable heating effects to the implanted surface). The laser system that was purchased for this work is the AccuScribe from New Wave Research, which uses a 355 nm Nd:YAG laser.

The scribing recommendations come from the unique problems associated with dividing the Genesis collectors: the large thickness of the samples (500-700 μm); the scribe must allow separation of the sample such that cleavage would be along the desired path of the scribe, regardless of any preferential crystallographic planes within the material (scribing along such a plane would be the most ideal scenario however); the fact they cannot be handled outside of a clean room. Laser scribing was also considered to be the least damaging procedure for the subdivision of the more complex layered collectors present on the arrays [2].

It was proposed that the laser would eventually be modified to include a mobile clean enclosure to allow transmission of the laser and subdivision of the samples under a controlled environment of known cleanliness. This enclosure was to replace the sample chamber on the machine, and be removable so as to allow transportation of the samples from the clean room to the laser scriber. This would allow the cleanliness of the clean room ('Class 10' or less than 10 particles of dust per cubic foot) to be maintained up until the beginning of the scribing operations.

Protocols were to be developed to scribe the collectors to minimize material waste, cutting debris and heating of the implanted side. If the implanted side were to be heated excessively by the cutting technique then it was feared the implanted species (~10 nm band near the surface) would diffuse into the collector wafer (500-700 μm in thickness), and be below the threshold for detection.

In order to decide on suitable protocols, the various parameters associated with the scribing were investigated using 500 μm thick silicon wafers (the majority of the collector arrays were Si). The effects of the parameters such as the speed of scribing, the depth of material removed per pass, etc. were evaluated with respect to the goals of the study as set out above.

3.1 AccuScribe System Operation

The AccuScribe system (pictured in *Fig 3.1*) employs a 355 nm Nd:YAG laser to ablate material from the surface of the substrate in a very precise and controlled fashion. The laser beam is focused to a point on the material surface, delivering a very large amount of energy to a very small area, thus heating up the material and ejecting it from the surface. The material is essentially vaporized into a plasma-like plume of debris. This plume may contain molecular fragments, free electrons, and ions from the substrate. The plume of debris is very likely to condense on the surface of the substrate around the scribed area if sufficient steps are not taken to remove the plume as it is formed. The stage beneath the laser (pictured in *Fig 3.2*) moves the sample along pre-programmed paths to produce the desired scribing pattern. The debris created by the scribing procedure is removed by means of a directed vacuum nozzles placed near the sample surface, as can be seen in *Fig 3.2*. The laser makes several passes to complete a scribe to desired depth in the material. Between each pass the stage is moved vertically by a fixed amount to bring the newly created surface at the bottom of the scribed line into the focal point of the laser beam. The process is then repeated, until the scribe reaches the required depth.

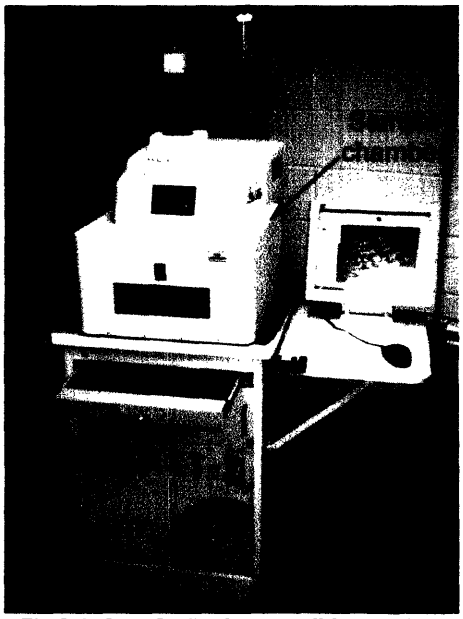

Fig 3.1: AccuScribe laser scribing system

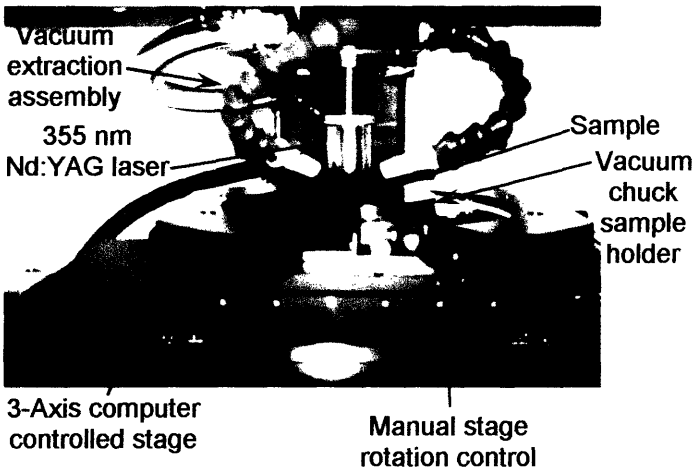

Fig 3.2: AccuScribe stage assembly

Initial tests produced fairly satisfactory scribes on the surface of silicon. The initial tests were performed on surplus material, which was polycrystalline silicon, rather than the single crystal material used on Genesis. This material was considered a reasonable choice for the initial testing and 'tuning' of the AccuScribe due to its relative abundance and low cost, and that grain boundaries are very unlikely to affect the ability to ablate material from the substrate. The important difference would be seen when it was required to fracture the specimens along the scribed lines – polycrystalline silicon and single crystal silicon would have different fracture mechanisms. The remainder of this section gives an overview of the typical scribes produced by the AccuScribe system and the issues which must be addressed in the optimization of the scribing parameters.

One of the first observations made of the scribed lines was the 'flare effect' at the beginning of each scribed path. This is shown in *Fig 3.3*. After consultation with New Wave, the effect was attributed to the laser firing at a higher initial intensity, and then equilibrating before moving on to the rest of the scribe.

The system has optical edge-detection, however this was found to be unreliable due to edge irregularities on the sample (most of the samples had a slightly beveled edge causing

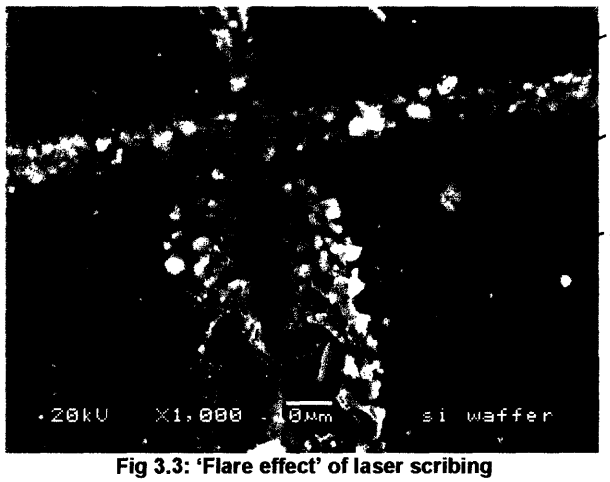

Fig 3.3: 'Flare effect' of laser scribing

unpredictable activation of the detection threshold). For this reason, and to avoid the flare effect causing excessive debris it was decided that future scribes would be extended off the edges of the sample to ensure the laser is in an optimal state at all times when in contact with the sample.

Fig 3.4 shows a cross-section of a typical scribed line after it has been fractured along the scribe path. The line was scribed at 1 mms^{-1}, and a 10 µm/pass *z*-axis increment.

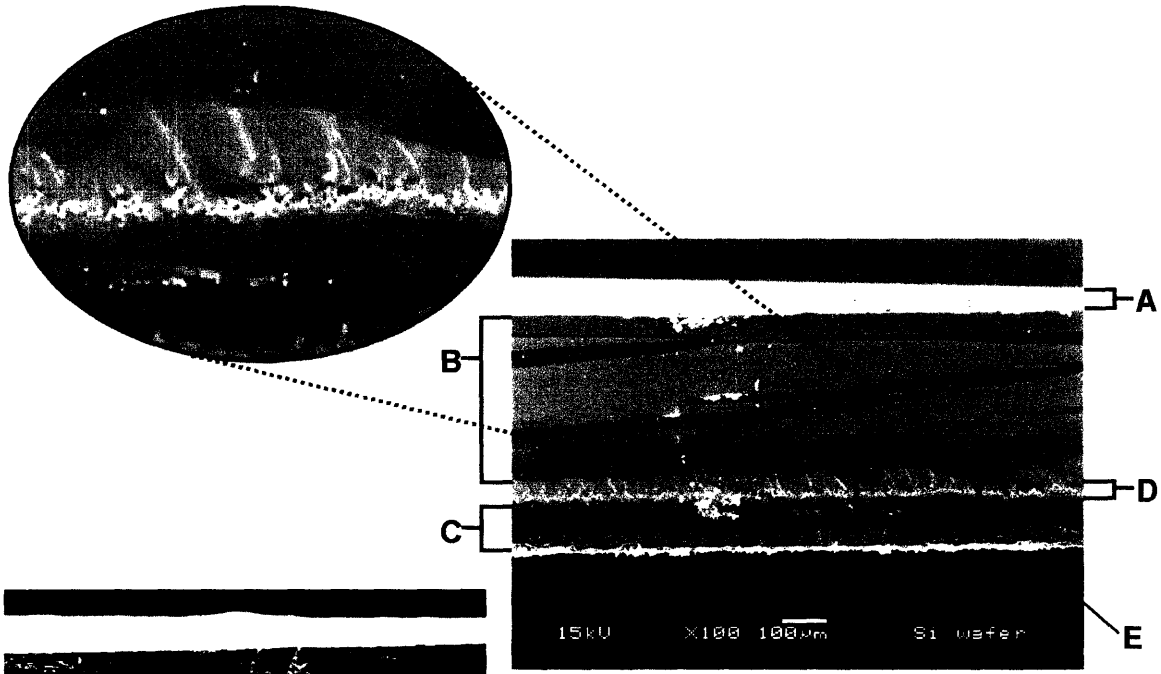

Fig 3.4(a): Cross-section of scribed line fractured along scribe path (poly crystalline Si)

Fig 3.4(b): Illustration of fracture surface for single crystal Si

Five distinct regions are identified in *Fig 3.4*:

- *Region A:* Reflection from surface of sample – sample not mounted perfectly vertically.
- *Region B:* This is the bulk region of the fracture. In (a) the fracture was of a polycrystalline sample. The dark striations visible correspond to fracture on the (111) planes of the different crystals through the sample ((111) is the primary slip plane in Si), producing steps on the fracture surface as shown. The fracture on a single crystal sample of Si shown in (b) displays the characteristic pattern of a simple cleavage fracture. The surface displays the characteristic *river pattern* of steps in the fracture surface. This is commonly caused by a cleavage crack crossing a screw dislocation within the Si crystal, producing a large step in the cleavage plane. These steps progressively run together to form steeper and steeper steps as seen in the pattern. The river pattern may also be caused by the initial crack in the crystal surface caused by the scribe aligning itself to follow the primary cleavage plane of the Si [35].
- *Region C:* This is a cross-section through the scribe line. The lighter region towards the top of the scribe (bottom of image) is due to debris ejected from the scribe but not able to be removed completely by the vacuum system. This debris then falls back on the sample. The majority of it is deposited either side of the scribed line (*Region E*), but some is likely to be deposited back into the scribed line as shown here.
- *Region D:* This region extends below the trough of the scribe for ~30μm into the sample. This is a common occurrence in laser ablation techniques where the laser heats up very small localised areas of material in the trough of the scribe, and ejects them. Hence the pitted appearance of the trough. The discoloured region below the pits shows the extent of the laser's heating below the trough of the scribe. This is termed the *heat affected zone* (*HAZ*), and is an important consideration when using the laser to scribe near through thickness of the actual collector arrays.
- *Region E:* This shows the build-up of debris on the surface of the Si, around the edges of the scribed line.

Another issue with the AccuScribe was the optimisation of the vacuum system used to remove the debris from the scribe path during operation. *Fig 3.5* shows the effect of the vacuum system.

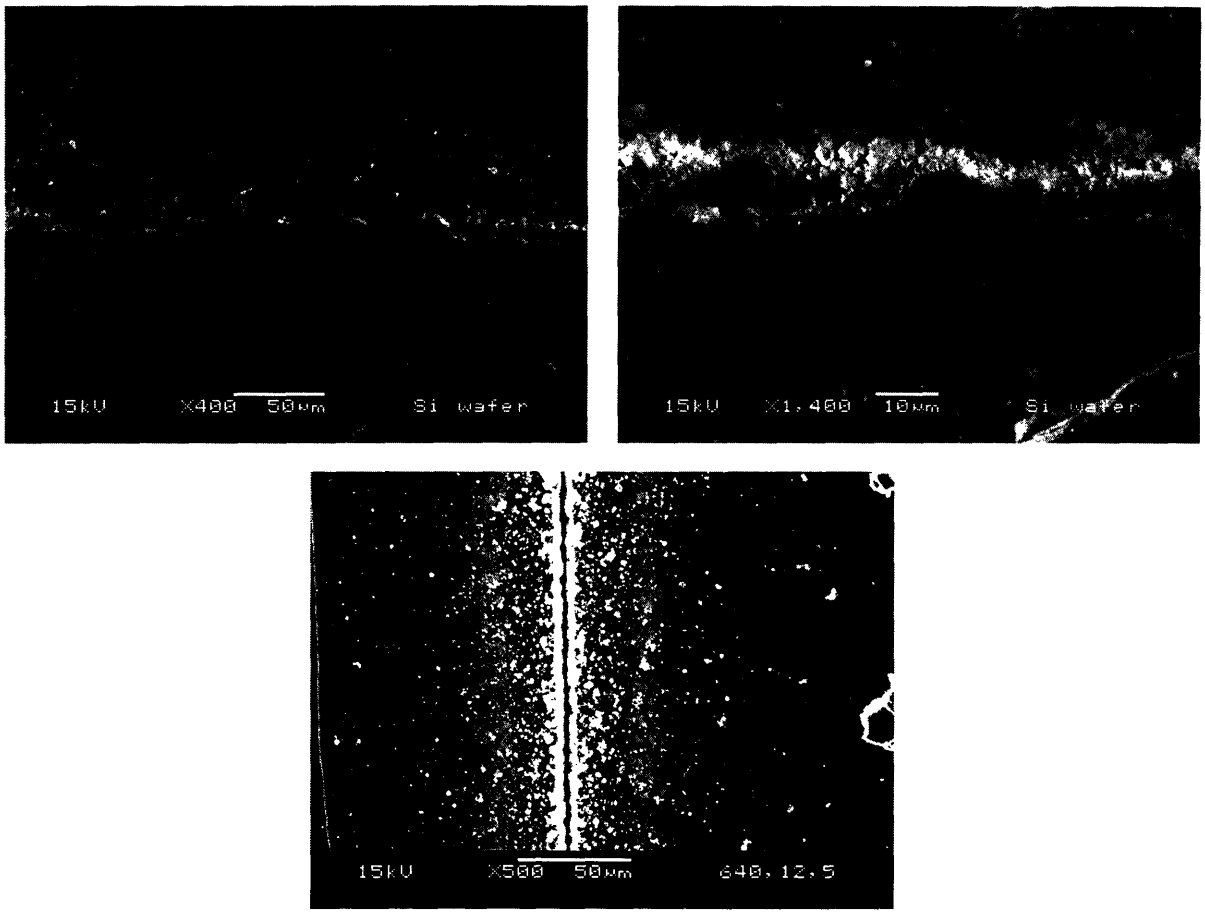

Fig 3.5: Scribes performed without [Top] and with [Bottom] the vacuum system active

The top two photos were taken of a scribe that was made without the vacuum system active, and the bottom photo was taken with the system running at its optimum level. It can clearly be seen that the vacuum system acts so as to draw the debris out of the crack, depositing some at the sides of the scribe, and extracting a small portion. It is important to draw the debris out of the scribe path, as some of the debris may be molten, or at least semi-solid. Debris particles such as these could potentially stick to the inner walls of the scribe and form small bridging bonds, making fracture along the scribe more difficult.

The references made to the 'optimum' operation of the vacuum system refer to the correct choice of *(i) vacuum source* and *(ii) vacuum nozzle*:

i. The vacuum pump supplied with the AccuScribe system was unsuitable as when the pump was active it caused significant vibration of the sample and stage, making accurate scribing impossible. A series of replacement pumps were tried, including a turbopump and a conventional vacuum cleaner. The vacuum cleaner was finally selected, as it produced the strongest vacuum suction, and hence would be the most efficient at drawing debris out of the scribe. The turbopump, although technically capable of pulling a higher vacuum, was designed to do so for a sealed chamber – it was not designed to be operated in a manner such as this (chamber open to air), and hence did not perform satisfactorily. The vacuum cleaner was found to pull a strong vacuum and the airflow steady enough so as not to affect the sample on the stage.

ii. The nozzles supplied with vacuum system were mounted on the tips of three positionable vacuum hoses (see *Fig 3.2*). The hoses were placed as close to the sample surface as possible was possible without making contact with it (~ 2 mm). The supplied nozzles were simply large diameter openings (~1 cm). In an effort to improve the efficiency of the vacuum system, several variations of the end-nozzles were procured. The aim of these nozzles was to better aim the vacuum at the surface of the sample. It was thought a smaller diameter opening would pull a higher specific vacuum, by pulling the same suction force on a smaller area of air. This would help to better extract the debris form the sample as it is produced. The dimensions of these nozzles can be seen in *Fig 3.6*.

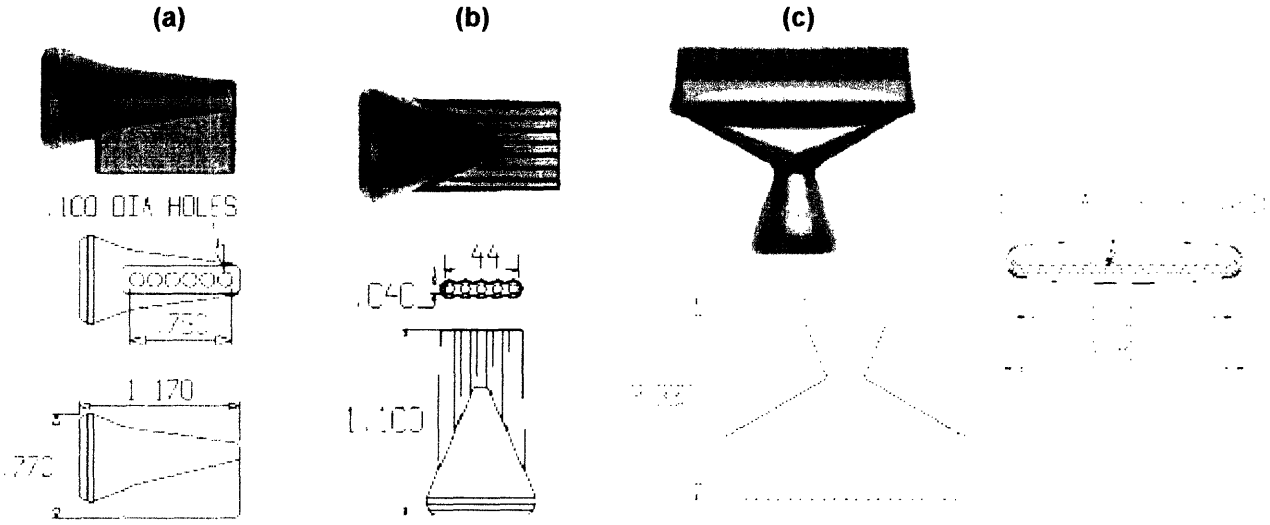

Fig 3.6: End-nozzles for Vacuum System: (a) 90-Deg. Spray Bar, (b) Flat 7, (c) Swivel 75

The efficiency of each of the nozzles was tested by scribing lines at various scribing speeds (1, 3, 5, 7, 10, and 18.8 mm s^{-1}) for a constant number of passes (30 passes – chosen to decrease time taken for experimentation, but produce reasonable results) and a constant value for *z*-increment per pass (5 µm/pass – considered to be a good conservative estimate for the amount of material removed per scribe based on initial observations). The scribed surfaces of the samples were then observed in the SEM, and the quantity and distribution of debris as a function of cut speed and nozzle type was observed.

Slightly less debris is observed with the faster scribing speeds. This is illustrated by *Fig 3.7*, which shows two lines, each scribed using the 90-Deg. Spray Bar, one at 1 mm s^{-1} and one at 18.8 mm s^{-1}. The effect of scribing speed on the amount of debris produced is investigated further in a later section.

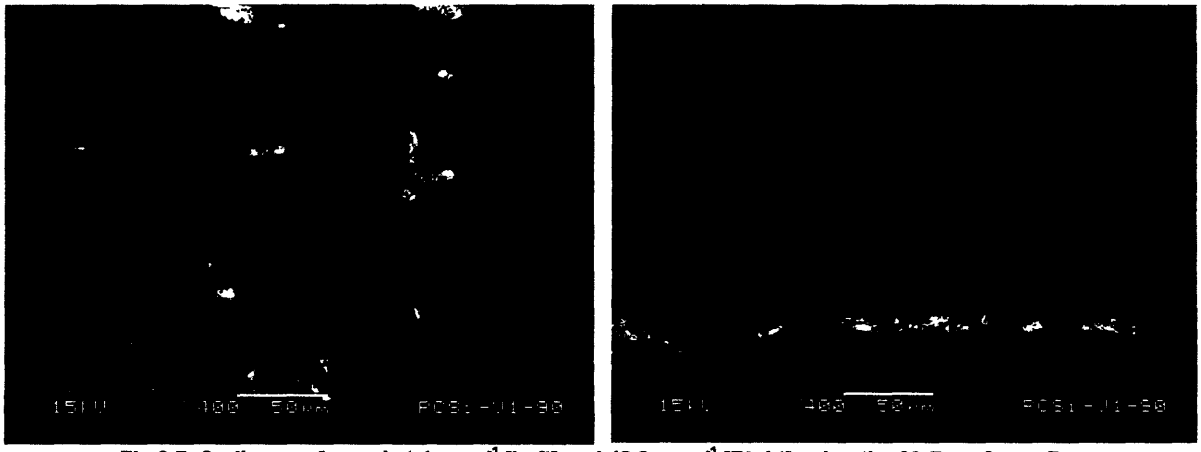

Fig 3.7: Scribes performed at 1 mms^{-1} [Left] and 18.8 mms^{-1} [Right] using the 90-Deg. Spray Bar

Overall the Flat 7 nozzle gave the best results – i.e. scribes made with this nozzle in place showed the least debris and the cleanest cuts, as shown in *Fig 3.8.*

Thus the 'optimal' vacuum system uses a conventional vacuum cleaner as the vacuum source and the Flat 7 nozzles on the ends of the vacuum hoses.

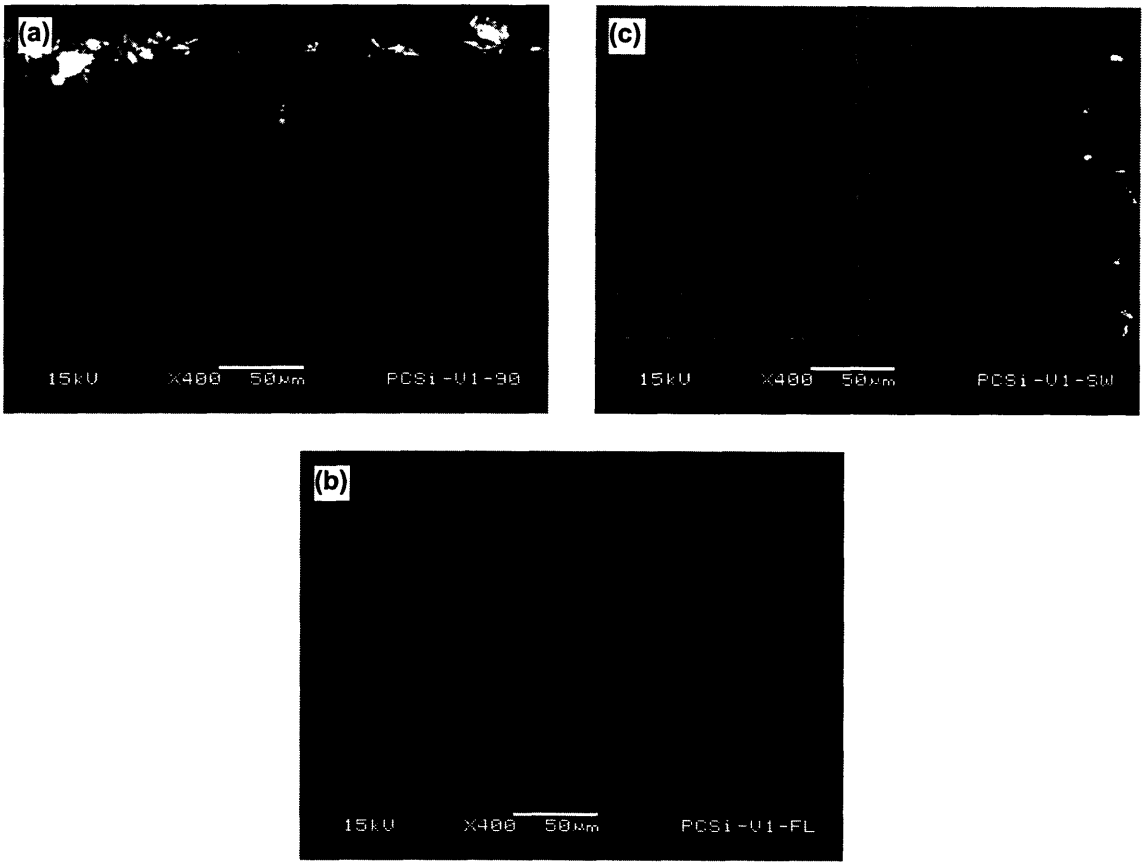

Fig 3.8: Scribes performed @ 10mms^{-1}, using the 90 Deg. Spray Bar (a), Flat 7 (b), Swivel 75 (c)

3.2 Chemical Etching of Wafers

An important consideration when cleaving the samples is the crystallographic symmetry of the material. The initial tests were performed on Si because it has a well understood fracture behaviour. Cleavage occurs most readily along close packed planes. Of the close packed planes slip occurs the most readily on those with the greatest number of independent slip directions. The aim of optimizing the scribing parameters is to cause eventual fracture along the scribe line, and it would obviously be desirable to utilize the symmetry of the material to aid in this.

Si has tetrahedral symmetry similar to diamond but with a larger lattice spacing. The primary slip system operates on the (111) planes. However, the wafer supplied to us, and those on the collector arrays are oriented with the (100) planes parallel to the surface of the wafer. Thus cleavage on the (111) planes is not desirable as it would produce pieces with beveled edges (the (111) plane would cleave at an angle of 45° to the surface). Thus for a cleave perpendicular to the surface another major plane of symmetry that may be utilized is the (110) planes. These are the desired cleavage planes for our application.

Analysis to verify the orientation of the Si wafers supplied to the Genesis mission was performed using XRD techniques. First a standard spectrum was taken for powdered Si to identify the peaks associated with the characteristic planes of symmetry in Si. The results are shown in *Fig 3.9*. Samples of both the single- and poly-crystalline Si used were then placed in the

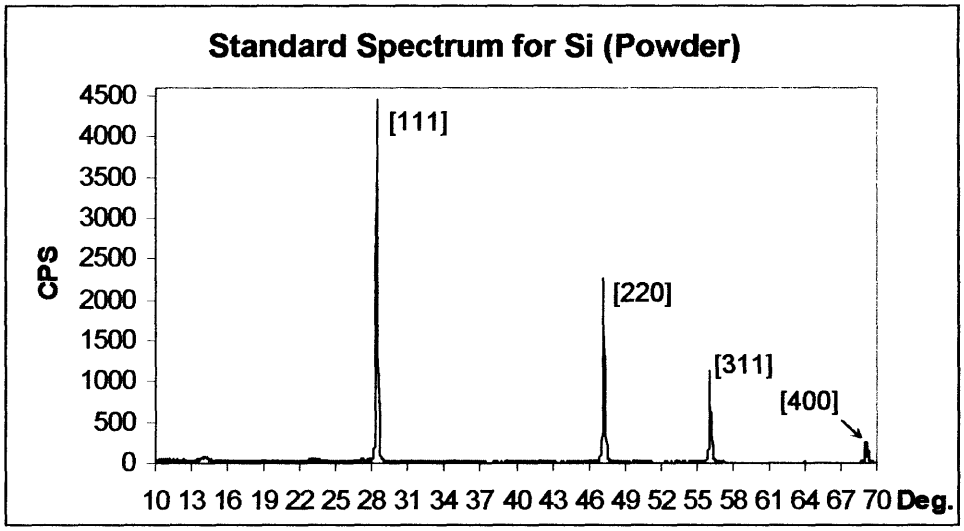

Fig 3.9: XRD Spectrum for Powdered Si

XRD. A spectrum of the single crystal sample was taken at a known orientation. The sample was then rotated 90 degrees and another spectrum taken. The poly crystalline sample was tested at only one orientation. The results of these tests can be seen in *Fig 3.10 – 3.12*. It can be seen form the spectra that the Si is indeed oriented so that the (100) planes (equivalent to (400)) are parallel to the surface of the wafer. The spectra for the single crystal sample are identical, showing the expected four-fold symmetry for the (100) planes within the wafer.

The polycrystalline spectrum shows that the polycrystal in use is an oriented polycrystal. The larger spread around the (400) peak is due to the sample being polycrystalline (larger scattering)., and could also be the result of a fine grain size (larger number of grain boundaries cause more scattering of the beam).

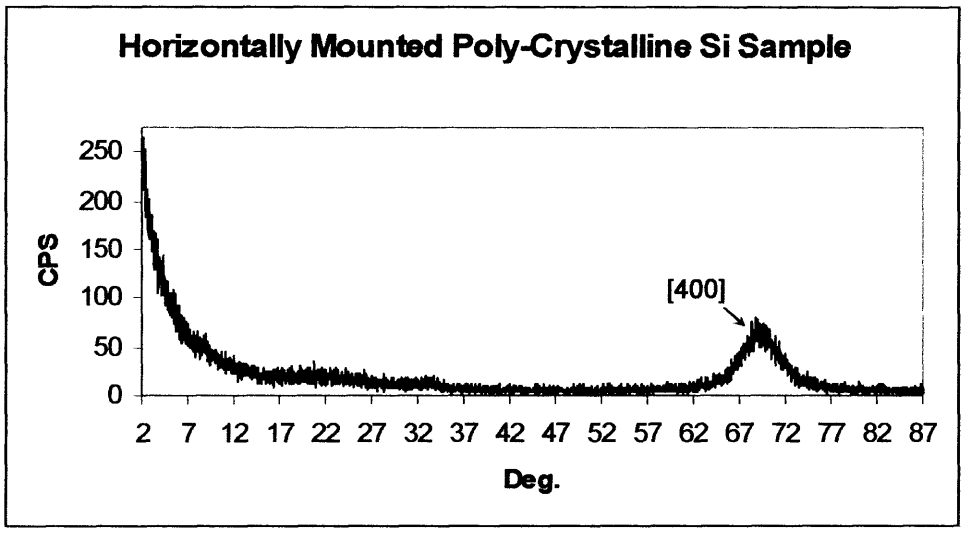

Fig 3.10: XRD Spectrum for Polycrystalline Si

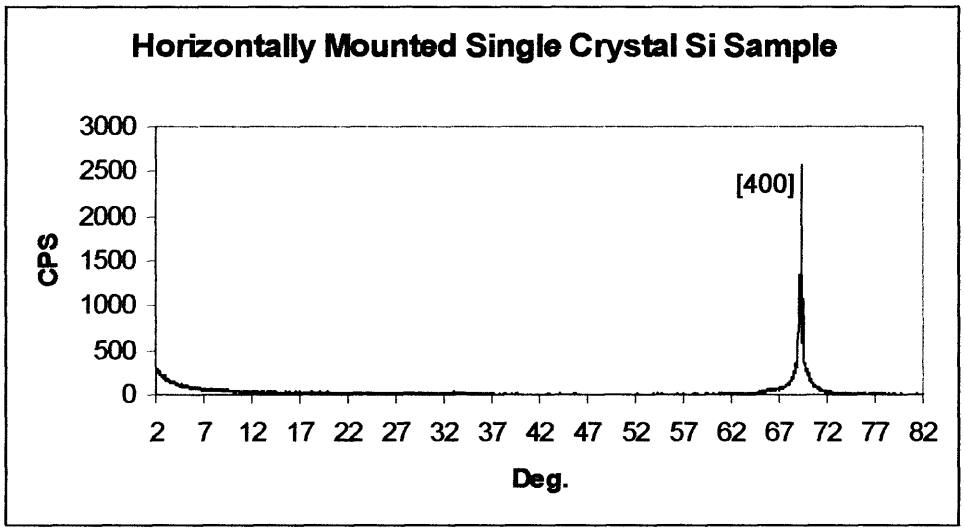

Fig 3.11: XRD Spectrum for Single Crystal Si of known orientation

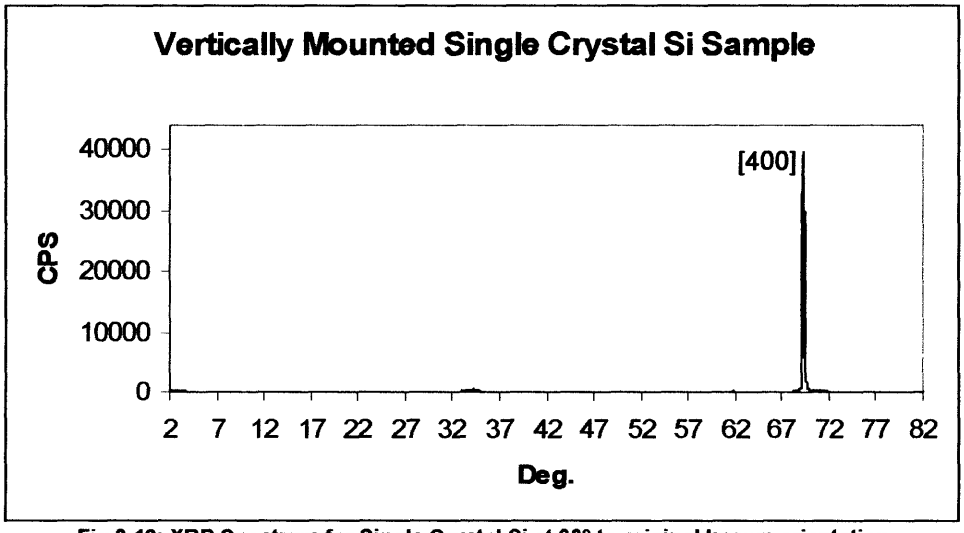

Fig 3.12: XRD Spectrum for Single Crystal Si at 90° to original known orientation

In order to promote cleavage along the (110) planes, the orientation of the planes with respect to the hexagonal collector wafer must be found. *Fig 3.13* shows a drawing of the design for the wafers. Note that the flat at the top corner was an allowable flat on any of the three 'sharp' corners. As such the 15° angle from the reference flat could refer to any one of three sides on any given collector plate. The original wafer was manufactured (by MEMC, Inc.) such that the (110) planes ran parallel and perpendicular to the reference flat of the wafer. However the orientation of the hexagon with respect to the original wafer was not preserved.

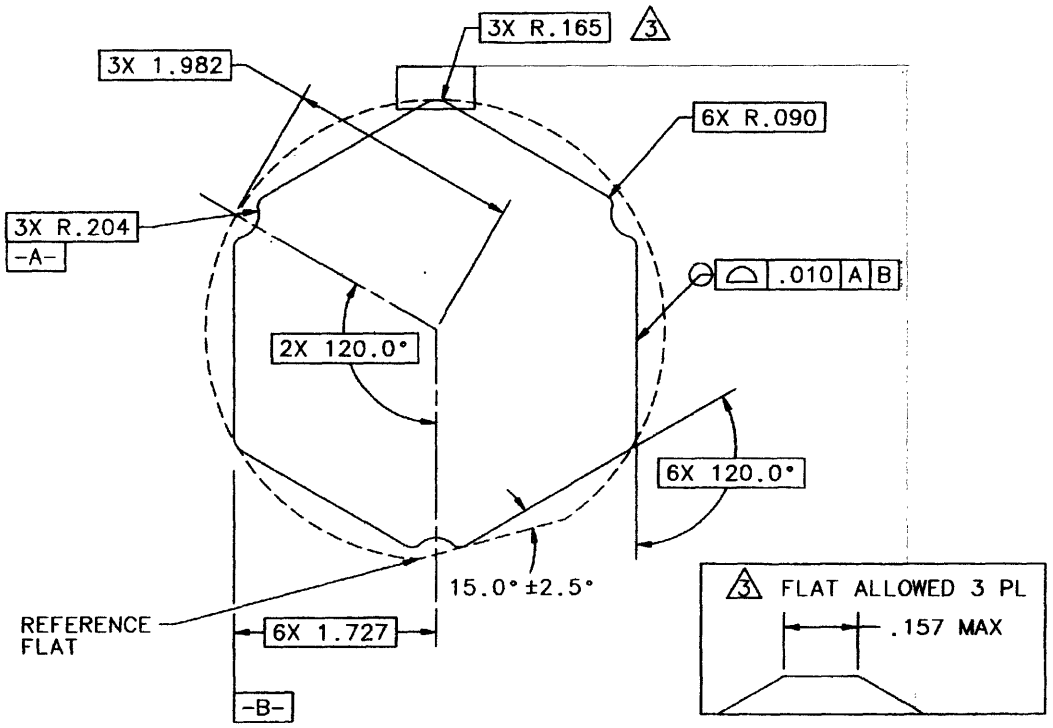

Fig 3.13: Dimensions of the Collector Array Hexagons

A system for identifying the orientation of the Si single crystal with respect to the edge of a given hexagon must be developed in order to orient samples to cleave along the (110) planes.

Chemical etching of a sacrificial fragment of material was the suggested way to determine the orientation of the wafer. A procedure for said etching found that suggested immersing the sample in *30% KOH* for *4 hours* [36]. The surface of the Si would preferentially be etched along the close packed planes, exposing them as parallel lines etched in the surface. The primary slip plane should etch the deepest.

Fig 3.14 shows the results of the test on a Si fragment. There are indeed etched lines visible on the surface of the Si wafer. They did not however bear much of a relation to the edge of the wafer. There were many other etched lines (much fainter) present on the surface. These could also be scratches on the surface of

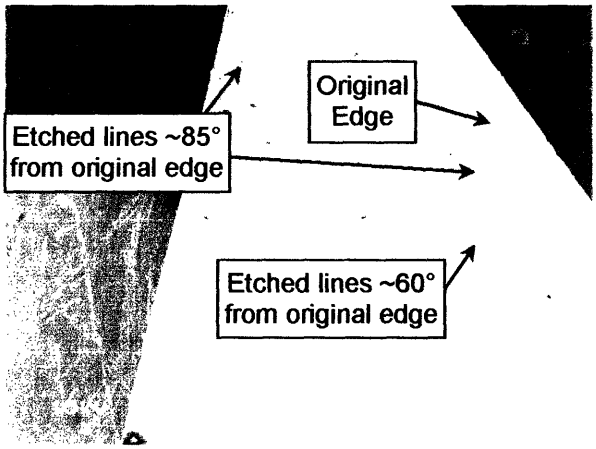

Fig 3.14: Etched lines present after 4 hours in 30% KOH

the wafer – the supposedly 'etched' lines labeled on *Fig 3.14* were not very much deeper than the array of seemingly random lines present elsewhere on the surface. It is more likely that the etched portions resulted from the etching of defects rather than an indication of crystallographic symmetry. Overall, the orientation of close packed planes cannot reliably be determined from this test.

The sample in *Fig 3.14* was returned to the KOH bath for a further 15 hours at room temperature. There was no visible change to the sample.

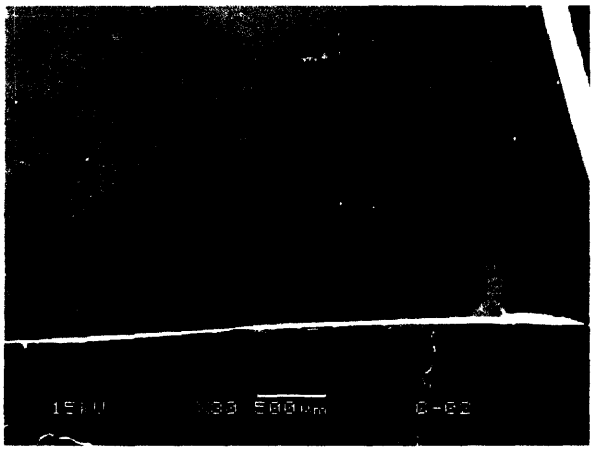

Fig 3.15: Results of immersion in 30% KOH for 1.5hrs @ 80°C

A further test was performed using 30% KOH and heating the bath to 80°C. The sample was immersed for 1.5 hours in the bath, and examined under an SEM, as shown in *Fig 3.15*. No lines were visible on the surface. This could have been because the elevated temperature was enough to allow the KOH to etch the entire surface away uniformly rather than limiting it to just the close packed planes. Again, this test proved to be inconclusive.

The idea was posed that if the surface of the Si was to be put in tension then this would aid cracking on the primary slip planes when the sample was exposed to the KOH bath. This was done by scribing short lines on the surface of the Si (10, 25, 50 and 100 passes were used at 5 mms^{-1} and 5 µm/pass z-inc.). The sample was then immersed in the 30% KOH bath at room temperature for 20 minutes, dried and placed in an oven, heated to 1000°C, and then allowed to cool to room temperature. This process was designed to mechanically and thermally stress the surface of the Si. Both poly- and single-crystal samples were tested in this way. Unfortunately the results were inconclusive with no clear etch lines visible on the surface.

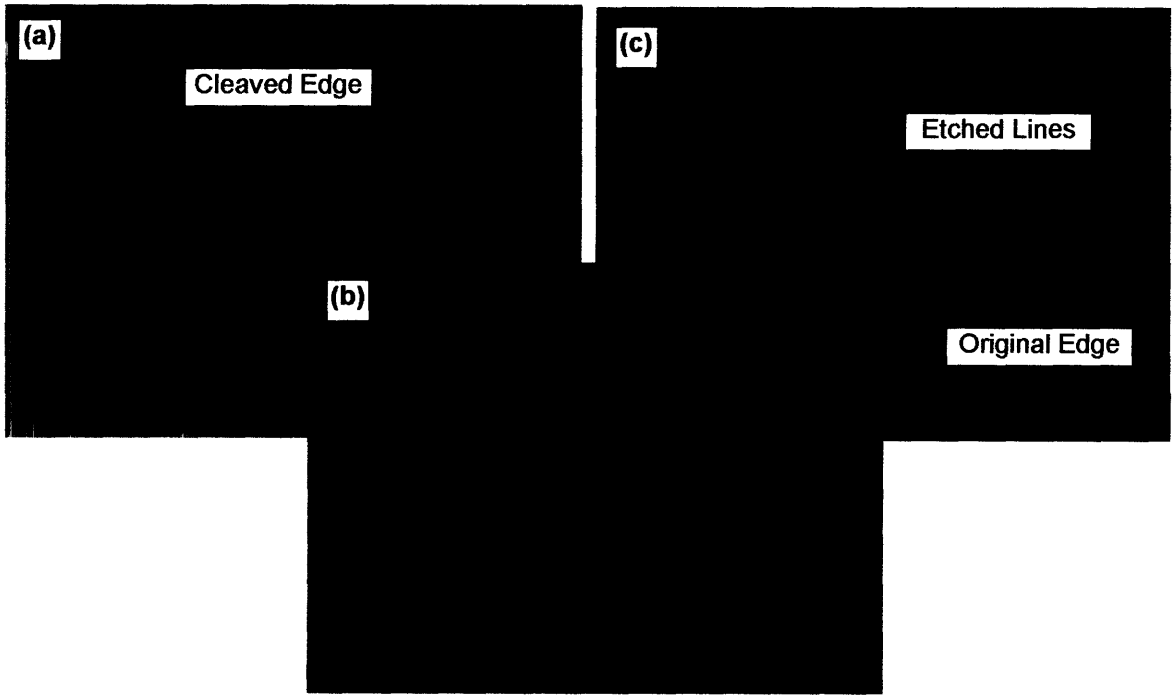

Fig 3.16: Etched lines present on surface of wafer as a result of exposure to HF and KOH (a), a close up of etched lines (b), and the orientation of the etched lines with respect to the true edge of the hexagon (c)

Dash [37] suggested a different approach be taken: the sample was first immersed in *HF*, and a mixture of *HF, nitric, and glacial acetic acid (1:3:10)* was added via an eye-dropper (until a reaction was observed at the surface). The reaction was allowed to continue for 1 minute before rinsing. On many of the samples silicon-tetraflouride formed on the surface of the sample. This was removed by placing in an ultrasonic bath with 30% KOH. The sample was then observed under the optical microscope, as shown in *Fig 3.16*.

Prominent etch lines can be seen even at a low magnification. These etched lines show too great a degree of symmetry to be random. They also appear to be oriented at roughly 90 degrees to the original edge of the specimen. These lines could be due to the etching of crystallographic planes. Alternatively they could be due to a manufacturing defect – a spot that was not polished adequately after the cutting of the wafer from the billet (the marks resemble abrasion scratches). However, there is insufficient information to decide exactly what the lines represent.

This technique in its current state does not allow reliable identification of the orientation of the Si wafers. The conclusions from this set of tests are that either scribing parameters that produce reliable cleaves independent of the orientation of the crystal, or a new technique for determining the orientation must be developed.

A further technique that could be employed is that of etch-pit analysis. This is based on the principle that where a dislocation intersects the surface of a crystal, the core of the dislocation etches more rapidly than the surrounding dislocation-free crystal. This results in a small etch pit that is large enough to be visible in an optical microscope [40]. The characteristic shape of an etch pit resulting from KOH etching of a (100) silicon surface is that of a square-based inverted pyramid. For a (100) oriented Si surface, the diagonals of the etch pits indicate the <100> direction, or in other words the (110) planes [41].

3.3 Variation of Cut Speed

The main goals of the scribing study were to minimize material wastage, and minimize the heating of the sample. Thus it would initially be desirable to scribe as quickly as possible so as to ablate as little material as possible (minimize material wastage), and obviously lower the amount of heating of the sample. However, if the cut speed were to be set too high, then the laser would not ablate sufficient material per pass to produce a scribe at all. Another consideration is that the laser beam must remain focused at the surface of the material to be scribed. Thus as each pass is made the material must be raised by a fixed amount so that the laser is incident on the new surface created by the previous scribe. If the scribe speed is too high, then the amount of material ablated will be less, and the material may be moved up into a position such that the beam is not incident at the actual new surface, but focused slightly below it. This effect would be made worse on each successive pass. In order to isolate the effect of the variation of cut speed, a fixed *z*-axis increment/pass (hereafter referred to as depth/pass) of 5 µm/pass was chosen. This was found to have produced well-defined scribes in preliminary observations. The number of passes used per scribe line in this test was set to 100 to ensure good penetration of the scribe into the silicon and well defined scribe edges for measurement of scribe width.

It can be seen that finding the optimal scribing speed is an important consideration. Experiments were performed over the full range of scribing speeds available on the AccuScribe, which allowed 1→18.8 mm s^{-1}. In order to quantify the success of the different scribing speeds used, measurements of cut width and depth of penetration were proposed. This was done by preparing specimens of a standard 5x10 mm size. On these specimens three separate lines were scribed for each cutting speed chosen. For each scribe the laser made 30 passes, and the Si was raised 5µm between each pass.

For each scribed line on the test specimens, a total of four measurements of cut width were made down the length of each line (observed under an SEM). A mean value for cut width was taken for each scribing speed (taking into account the three separate scribed lines), along with the standard deviation (calculated in the standard way, given by *Eqn. 3.1*). For the perposes of this study, 'cut width' is defined as being the distance from one edge of the debris line along the left edge of the scribe to the edge of the debris line on the right edge of the scribe (illustrated in *Fig 3.19*). A summary of the results obtained can be seen in *Table 3.1*, and graphically in *Fig 3.17*.

$$\sigma = \sqrt{\frac{\sum (X-\mu)^2}{N}}$$

Where :

σ = Standard Deviation

X = Variable

μ = Mean

N = Population Size

Eqn 3.1: Standard deviation of a population

Cut Speed Summary		
Speed (mms^{-1})	Cut Width (µm)	
	Mean (µm)	Std. Dev. (µm)
1	18.63	1.11
2	17.60	0.96
3	14.63	0.81
4	16.54	0.86
5	14.63	1.71
6	15.71	1.70
7	12.42	0.70
8	11.50	0.73
9	9.31	0.58
10	9.69	0.36
15	9.02	0.31
18.8	8.98	0.33

Table 3.1: Summary of Cut Speed Measurements

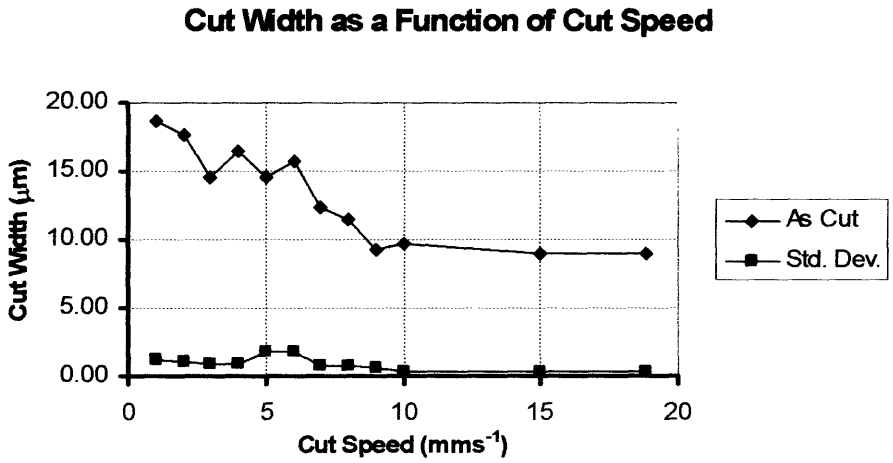

Fig 3.17: Summary of Cut Speed Measurements

It can clearly be seen from the cut speed measurements that an increase in cut speed does indeed decrease the width of the cut as suggested earlier. This gives significant evidence to support the theory that as the speed of the scribing increases, the laser is incident on a given area of the surface of the Si for a shorter time, thus removing less material overall. The standard deviation of the results is generally on the order of 0.8 µm for each reading, which accounts for the noise on the plot for the slower cutting speeds. The standard deviation can be seen to be higher for the 5 and 6 mm s^{-1} readings (~1.7 µm), and to decrease for the faster cutting speeds (~0.3 µm for >10 mm s^{-1}). This is due to the different nature of the debris formed with different cutting speeds – for the faster speeds the debris is finer and more evenly distributed, and the slower speeds deposit debris in coarse chunks (greater laser energy delivered per unit area of scribe means larger chunks of material may be removed). This can be seen in *Fig 3.18*. The reason for the larger standard deviation for the slower cut speeds is that the cut width is measured from one edge of the debris surrounding the scribe to the other; if the size of the debris chunks vary greatly along the length of the scribe (large chunks) so will the measured cut width. Conversely if the debris is finer, it is deposited in a more regular pattern along the scribe length, allowing more consistent width measurements to be made.

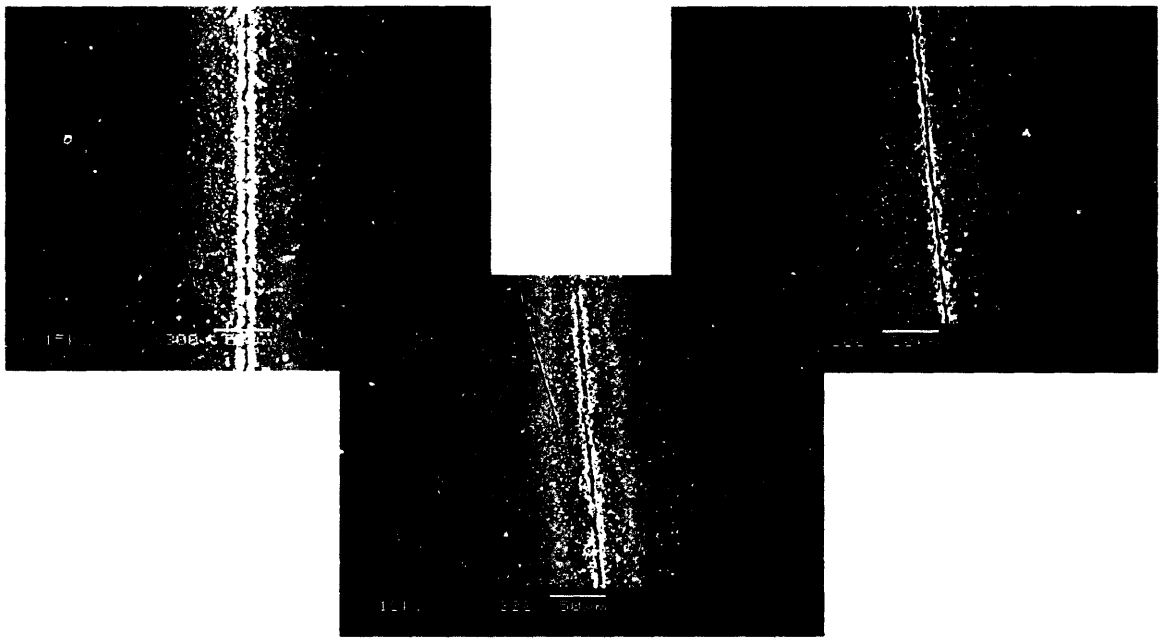

Fig 3.18: Selection of SEM images of Cut Speed Tests: 1 mms^{-1} [Left], 7 mms^{-1} [Centre], 18.8 mms^{-1} [Right]

A representative set of SEM micrographs for various cutting speeds is shown in *Fig 3.18*. They clearly show the decreasing cut width (indicated by the bright white corners of the scribe) with increasing cut speed. It is also worth noting here the appearance of the scribes – the scribe is accompanied by very visible stripes of debris each side of it. The debris appears white on the micrographs due to charging effects under the electron beam. The debris was investigated by electron dispersive spectroscopy (EDS), and a significant amount of oxygen was found to be present in the white areas, and none in the black areas (silicon base material). The only explanation for this would be the silicon had been oxidized by the heating of the laser during the ablation of material from the scribe lines. The extra heating would increase the rate of oxidation of the ablated silicon chunks significantly compared to that of the bulk material. The pattern observed in *Fig 3.*18 is also seen in many other photos used to make the cut width measurements, thus supporting this hypothesis. The debris created at the bottom of the scribe at each pass would be sucked up by the vacuum system. However it can be seen that only a certain percentage of the debris produced is able to be completely removed from the scribe, leaving a significant amount of debris deposited along the edges of the scribe. This produces the bright white stripes running parallel to the scribe line. A larger view of the 1 mms^{-1} scribe is shown in *Fig 3.19* to better illustrate this.

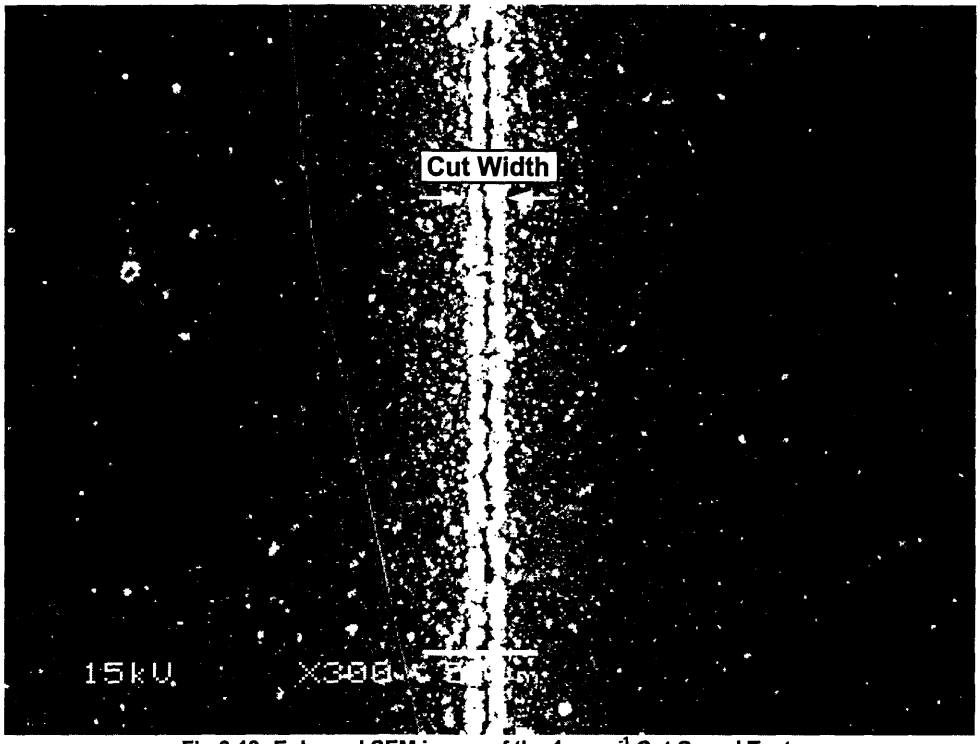

Fig 3.19: Enlarged SEM image of the 1 mms^{-1} Cut Speed Test

As observed for the chunks of debris, the white 'haze' either side of the scribe indicates regions of localized oxidation, and hence heating of the bulk silicon in this region. The 'haze' was an observation consistent across all images taken of the laser scribes. It has not been possible to assess the extent of oxidation through the thickness of the silicon at this time.

A better understanding of the cut width may be gained by cleaning the debris visible in the micrographs from the surface of the silicon, thus exposing the 'true' scribe edges.

The cleaning procedure for the samples was to immerse them in 30% KOH for 5 minutes and place them in an ultrasonic cleaner. The samples were then immersed in distilled water for one minute, again in the ultrasonic cleaner to rinse the KOH from the sample surface and prevent significant etching of the sample surface. The KOH removes both Si and SiO_2 with equal vigor, and it is important to halt this reaction before too much the surface of the Si is removed, which would otherwise destroy the scribe wall features that are of interest. The one minute rinse was

repeated three times for each sample. The results of these tests are summarized in *Table 3.2* and shown as a comparison with the original measurements in *Fig 3.17*.

Clean Cut Speed - Summary Table		
Speed (mms^{-1})	Cut Width (μm)	
	Mean (μm)	Std. Dev. (μm)
1	6.83	0.66
2	**7.10**	**0.84**
3	7.60	1.32
4	**7.28**	**1.21**
5	7.36	0.77
6	**8.11**	**0.80**
7	8.75	1.45
8	**9.94**	**1.08**
9	9.57	0.86
10	**9.27**	**0.58**
15		
18.8		

Table 3.2: Summary of Cut Width measurements on cleaned Cut Speed samples

It can be seen from *Fig 3.20* that once the samples are cleared of cutting debris there is not a significant or tangible variation of cut width with cut speed. The standard deviation does not show any distinct pattern, but is on average ~1 μm larger than for the as cut measurements. This is due

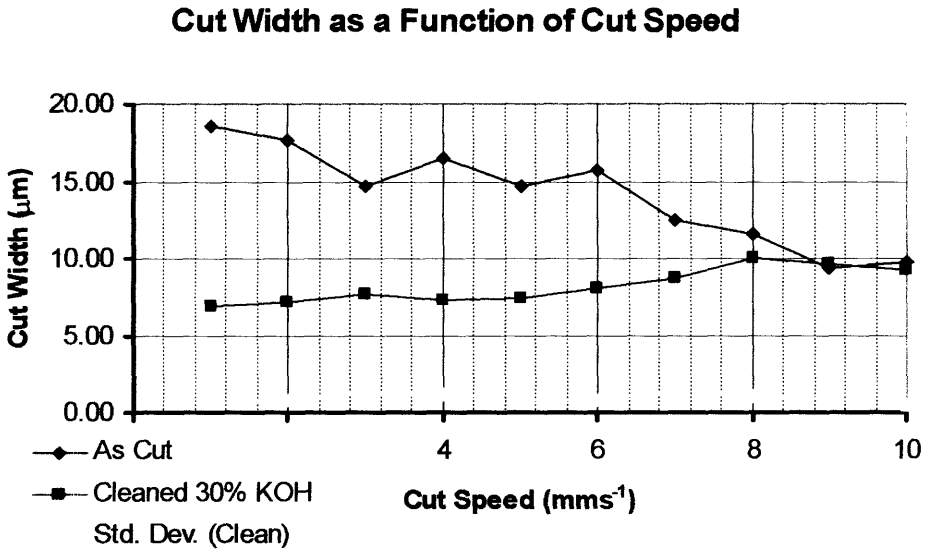

Fig 3.20: Comparison of 'Clean' and 'As Cut' Cut Widths Cut Speed samples

to the irregular edges of the exposed scribes, probably due to the etching procedure. However, the trend observed before the debris was removed is still a useful observation. The amount of debris surrounding a scribe line is indicative of the amount of material removed. Therefore it can be said that variation in 'cut width' observed prior to debris cleaning must be as a result of a variation in the depth of the scribe in the silicon. Therefore it may still be said that for a faster cut speed a smaller amount of material is removed. The faster cut speeds produce shallower scribes than the slow cut speeds.

Fig 3.21 highlights some interesting features about the scribe. It can be seen that there is a definite region of damage around the edge of the scribe lines, rather than there being a sharp

edge. This suggests that the debris that has been removed by cleaning also removed some of the Si around the edge of the crack. This means that the debris must have been strongly bonded to the material beneath, possibly because the debris was in a molten or semi-solid state when ejected from the scribe. The second interesting observation is that the white 'haze' observed in all of the samples so far either side of the scribe line is still present. This means that the effect is not simply due to fine debris deposited on the surface of the sample, but is due to the laser heating. The amount of material affected by the laser scribing is not limited to simply the width of the scribed line, but extends 30-35μm each side of the scribed line. The depth to which this effect is present is not known at this time.

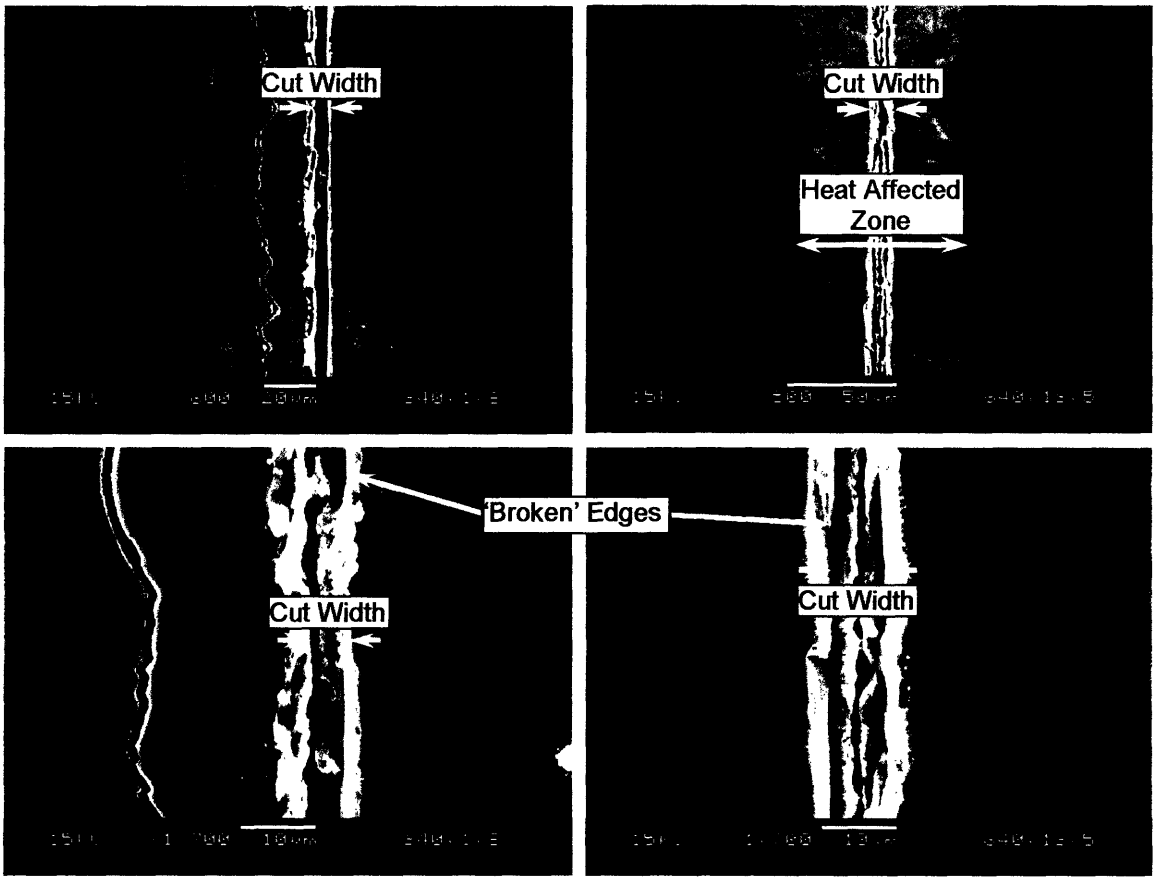

Fig 3.21: Observations of Cleaned Samples

There is a distinct trend visible in the intensity of the observed HAZ for the different cut speeds. *Fig 3.22* shows a selection of the images taken of the cleaned cut speed samples. The figure shows that for increasing cut speed the charging effect is less, giving a less intense haze. The width of the HAZ appears to be reasonably constant for each of the scribing speeds displayed in *Fig 3.22*. This can easily be explained by the fact that the faster cutting speeds result in less heat input from the laser, and hence the oxidation effects will be less. The trend of decreasing intensity of the haze observed for the faster speeds is a direct result of the extent of oxidation caused by laser heating.

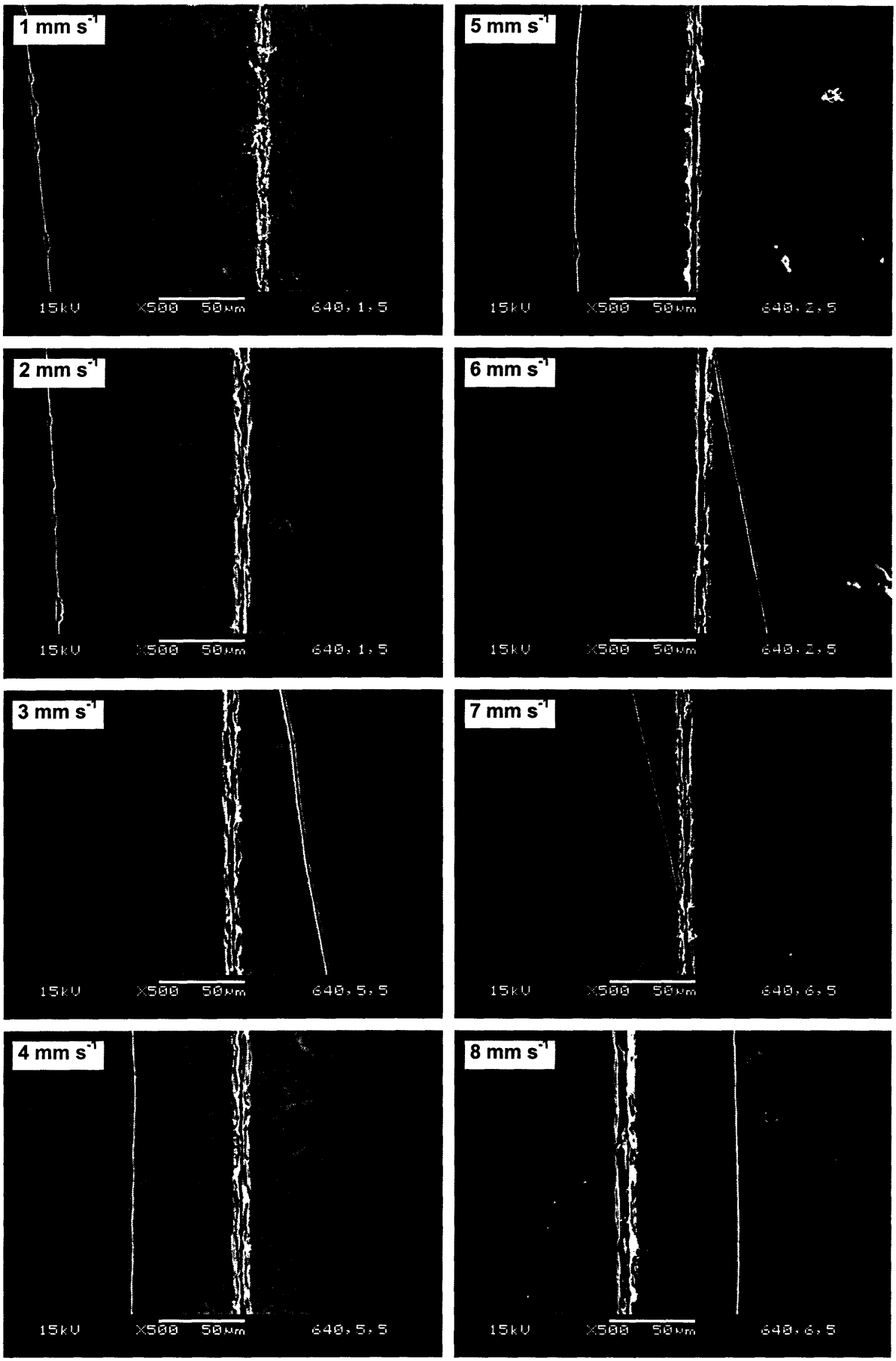

Fig 3.22: SEM Micrographs of clean cut speed samples, showing effect of cut speed on the HAZ

In order to fully quantify the 'success' of each of the cut speeds, measurement of the depth of scribe produced must be made. The main complication with this is that the scribes produced did not breach the ends of the sample. The samples must be polished down to a level so as to expose the scribe profile on one edge for observation in the SEM. Measurements of scribe depth may then be taken for each scribed line. Due to the events of September 8th 2004, these experiments were not performed.

However, in lieu of these experiments to directly measure the depth, the scribe width was found to be roughly independent of the cut speed, but the amount of material removed was shown to decrease for an increased cutting speed. So for a constant width of scribe, the larger amount of debris must represent a deeper scribe penetration. The extent to which the material surrounding the scribe lines is heated is less for the faster cut speeds. Hence a faster scribing speed is favourable in terms of minimizing the heating effects of the scribing process on the samples.

The observations made above seem to favour higher scribing speeds in the interest of minimizing material wastage and heating effects, but must be balanced by the tendency to produce an increasingly shallower scribe with increasing cut speed.

3.4 Depth per Pass

This was the next logical parameter to vary. The laser ideally should always be focused on the surface of the material to be removed. As the scribing process progresses successive layers of material are removed in the path of the scribe. The stage is set to move vertically upwards by a fixed amount after each pass to bring the laser into focus with the new surface created at the bottom of the scribe by the previous pass. Optimisation of this parameter is essential as if the laser beam was not moved so as to be in focus at the bottom of the scribe, but instead focused somewhere within the scribe trough above the scribe surface or at a point inside the Si below the trough, then less than the maximum amount of material would be removed in the following scribe. If the laser was focused at a point other than the new material surface, then a significant portion of the laser energy would go to simply heating the sample, rather than ablating away new material. If the depth per pass is set to a less than optimal value the laser will move further and further out of focus with the new material surface each pass. One of the main aims of the development of the scribing parameters is to minimize the non-essential heating of the samples. Hence otpimisation of the depth of z-axis increment per pass is essential.

It is expected that there is an optimum value for this parameter. This may be quantified by performing tests to examine the cut widths and depths produced by various values for the depth of z-axis increment per pass. For a fixed scribing speed, it is expected that there will be a constant cut width (as suggested by the previous section). However, the amount of material removed per pass will be larger for values of depth per pass closer to the optimum. This material will be deposited along the sides of the scribed lines, obscuring the actual edges of the scribe. This may give an artificially large value for cut width for depth per pass values closer to the optimum, and could conceivably be used as an indicator for the optimum value.

The specimens used to test this parameter were the same as were used in the cut speed tests. The tests were conducted with a cut speed of 5 mm s^{-1}, and 100 passes were used. The width and depth values were also collected in the same way: three lines scribed per depth per pass value, and four measurements of cut width taken per line, and one of the depth of each line. Mean and standard deviation values were calculated as before. A summary of the results are shown in *Table 3.3*, and graphically in *Fig 3.23*.

Depth/Pass Summary		
Depth/Pass (μm)	Cut Width (μm)	
	Mean (μm)	Std. Dev. (μm)
1	14.23	1.09
2	**14.75**	**1.03**
3	12.63	2.50
4	**16.50**	**1.62**
5	18.08	1.38
6	**17.58**	**1.56**
7	15.04	1.56
8	**10.88**	**1.37**
9	11.67	1.50
10	**11.00**	**1.13**
11	14.25	2.31
12	**12.58**	**1.16**
15	12.17	1.59

Table 3.3: Summary of Depth/Pass results

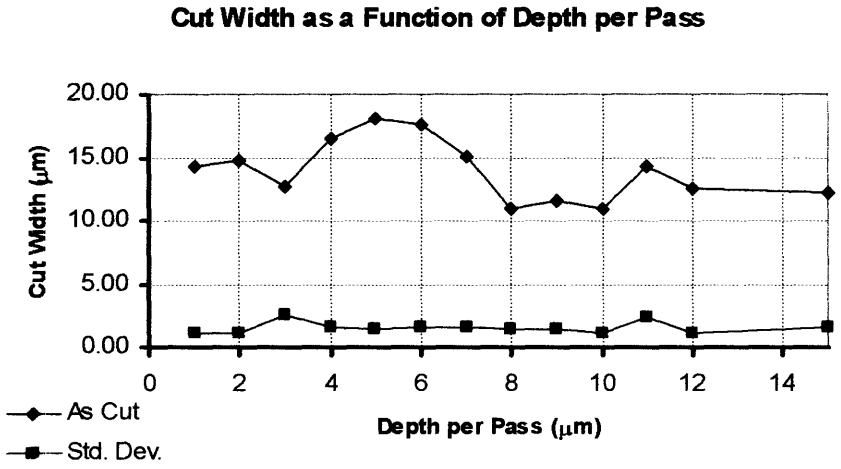

Fig 3.23: Summary of Depth/Pass results

It can be seen from *Fig 3.23* that there is indeed a peak of cut width, as predicted. The standard deviation is constant throughout, and shows no dependence on the depth per pass. *Fig 3.24* shows a comparison of the typical micrographs obtained from the 15μm/pass and the 5μm/pass samples. It can clearly be seen that there is significantly more debris present on the 5μm/pass sample than on the 15μm/pass sample. This supports the predication that there would be a peak in the amount of debris present on the sample surface for the optimal depth/pass setting. In order to conclude that the observation of a seemingly larger cut width for the 5μm/pass sample is in fact simply an observation of a greater amount of debris produced by a more optimized depth/pass setting, the samples must be cleaned of debris, and the measurements repeated.

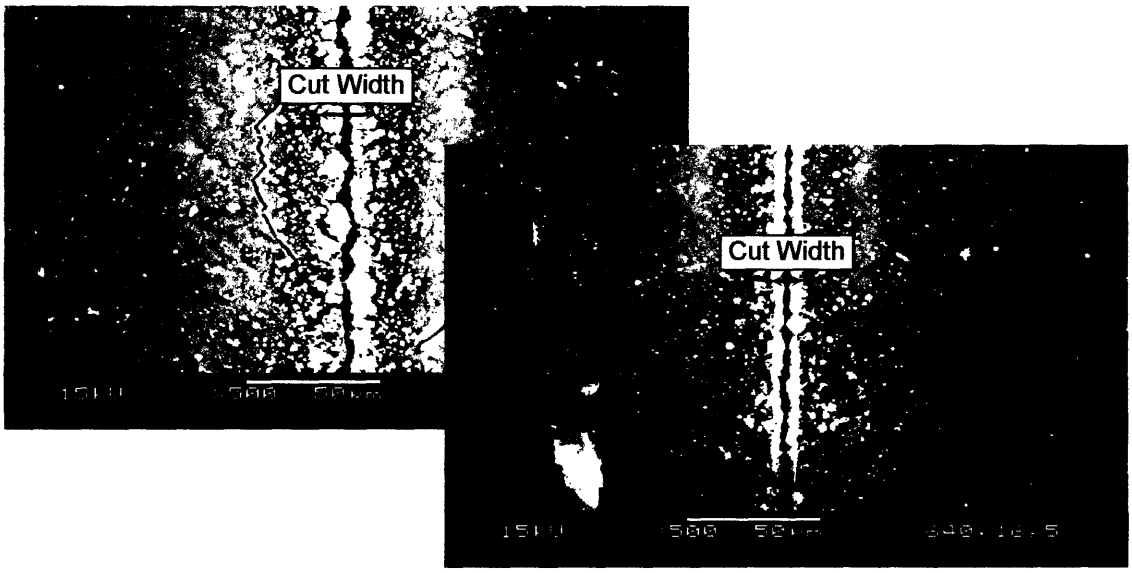

Fig 3.24: SEM Micrographs of 5 µm/pass sample [Left], and 15 µm/pass sample [Right]

The cleaning procedure for the samples was to immerse them in 30% KOH for 5 minutes and place them in an ultrasonic cleaner. The samples were then immersed in distilled water for one minute, again in the ultrasonic cleaner to rinse the KOH from the sample surface and prevent significant etching of the sample surface. The one minute rinse was repeated three times for each sample. The results of these tests are summarized in *Table 3.4* and shown as a comparison with the original measurements in *Fig 3.25*.

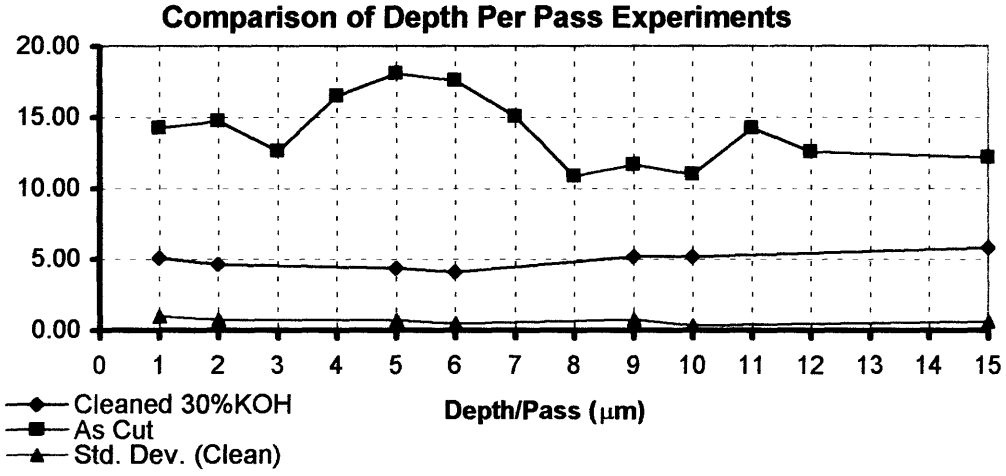

Fig 3.25: Comparison of 'As Cut' and 'Clean' Depth/Pass Samples

Not all of the samples were tested when clean, as time did not permit this. It can be seen from *Fig 3.25* that the cut width remains relatively constant with the variations in the depth/pass. The values for the cut widths after cleaning are much smaller, and their standard deviation is consistently small (~< 0.7 µm). This is because the removal of the debris allows direct measurement of the scribe edges. The cleaned depth/pass samples displayed the same characteristics as observed for the cut speed samples in *Fig 3.21.*

Clean Depth/Pass - Summary Table		
Depth/Pass (µm)	Cut Width (µm)	
	Mean (µm)	Std. Dev. (µm)
1	5.09	1.00
2	4.65	0.78
3		
4		
5	4.37	0.72
6	4.09	0.49
7		
8		
9	5.16	0.75
10	5.16	0.35
11		
12		
15	5.80	0.63

Table 3.4: Summary of Cut Width data for Cleaned Depth/Pass Samples

Fig 3.27 shows a selection of SEM images taken of the cleaned depth/pass samples. Particular

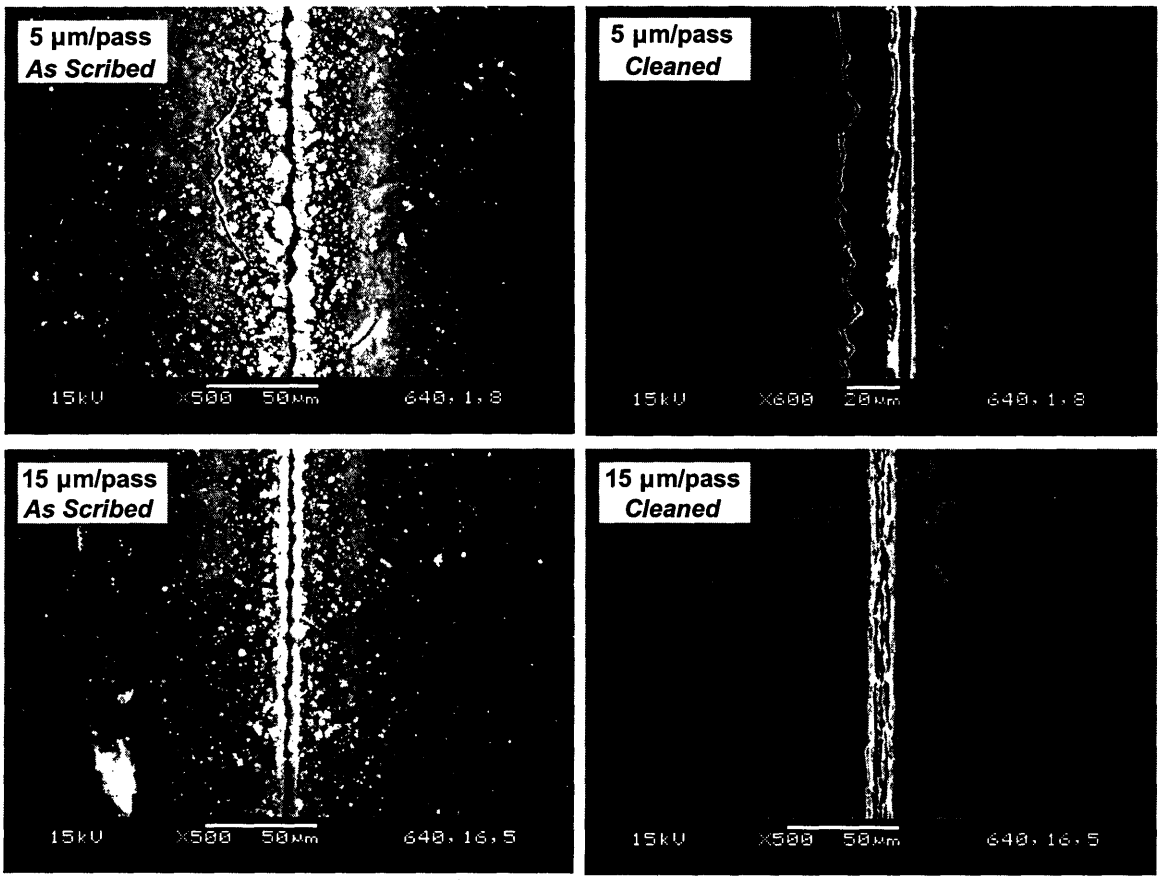

Fig 3.26: SEM Micrographs of 5 and 15 µm/pass samples before and after cleaning

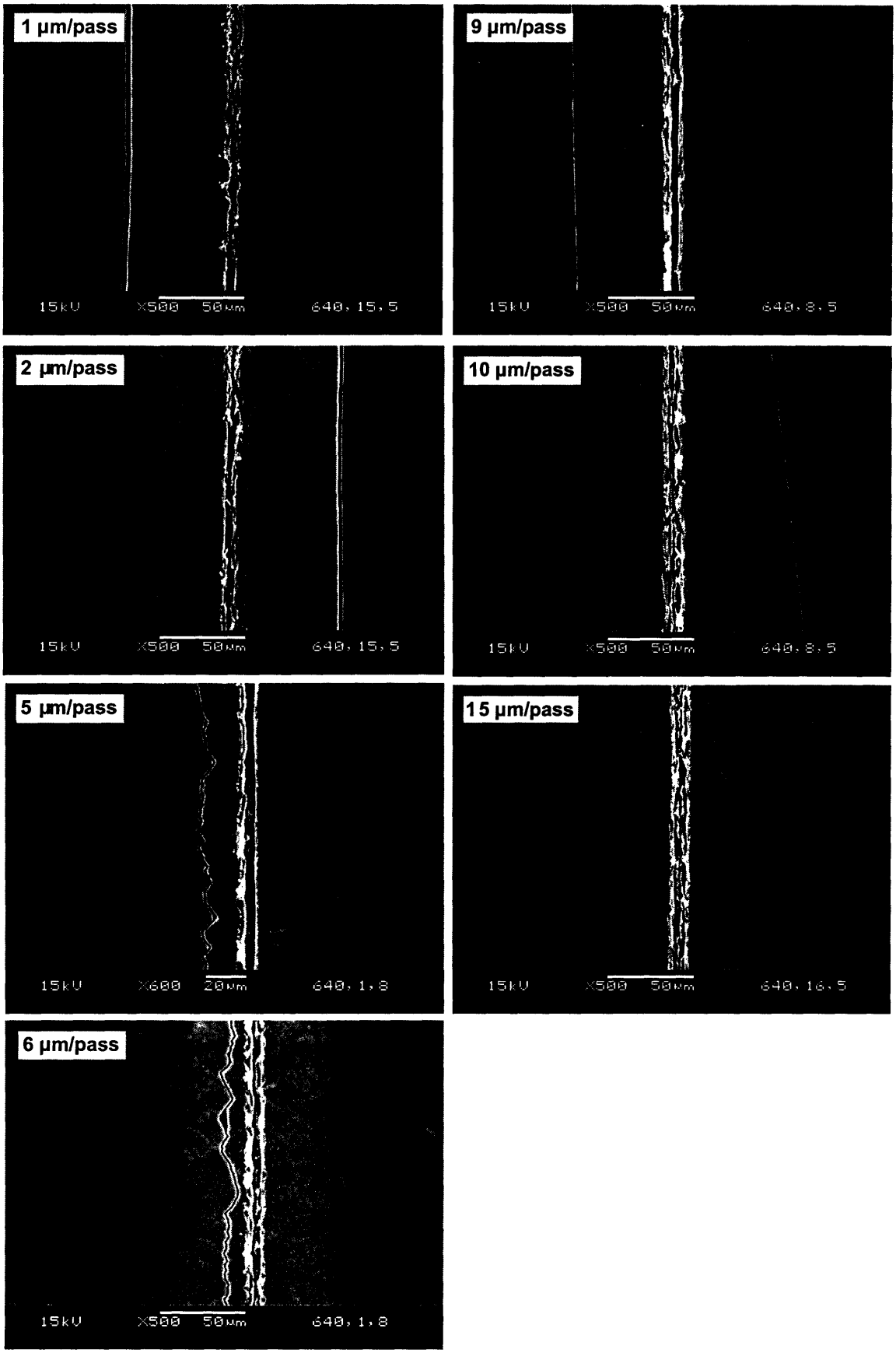

Fig 3.27: SEM micrographs of clean Depth/Pass samples, showing the effect of depth/pass on the HAZ

attention must be paid to the nature of the HAZ. It is apparent for the 1, 2, and 5 µm/pass images that the HAZ exists as two stripes separated from the scribe by seemingly unaffected Si. 6, 9, 10, and 15 µm/pass images show the HAZ as a continuous band each side of the scribe, and extending all the way to the edge of the scribe lines. This effect is due to the nature of the debris present on the Si surface prior to etching. *Fig 3.26* shows a comparison between the 5 and 15 µm/pass samples before and after etching.

Fig 3.25 shows for the 5 µm/pass sample that the debris surrounding the scribe is both plentiful and coarse in nature. As the laser is moved to focus on the trough of the scribe, the unfocused beam will be incident on the surface of the sample, and is schematically illustrated in *Fig 3.28* for the ideal case – laser focused perfectly on the trough of the scribe. It should be noted that this schematic has been verified as an accurate depiction of the laser operation by New Wave Research.

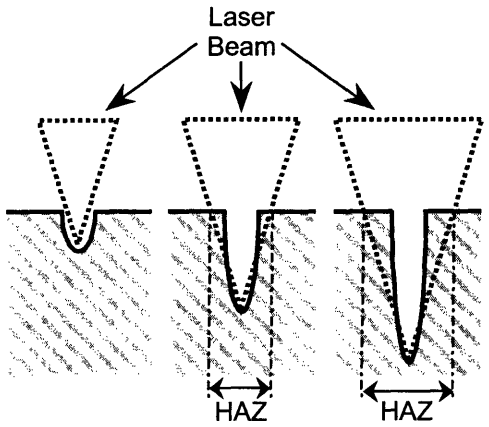

Fig 3.28: Development of Heat Affected Zone (HAZ) during scribing

The pattern of the HAZ observed in *Fig 3.26* for the cleaned 5 µm/pass sample may be explained by the debris visible on the uncleaned sample shielding the surface of the Si from the heat of the laser: note the intense white glow of the debris, indicating much heating, in contrast to the relatively dark Si substrate visible behind the debris. Thus when the debris is etched away from the surface the unheated (relatively) Si surface is exposed as dark bands either side of the scribe. The edges of the scribe can still be seen to be white. This is due to the large 'globules' of debris present that were present on the edges of the scribe prior to etching. These debris particles form an almost continuous band along the edge of the scribe, and therefore are able to conduct the heat from the unfocused laser more effectively down to the Si surface in the region immediately adjacent to the scribe. Hence the white region visible in the cleaned sample in this location. For the 15 µm/pass sample, much less debris is present, and it is much finer in nature (see *Fig 3.26*). This does not shield the surface of the Si as effectively, allowing the heating of the unfocused laser beam to heat the surface of the Si more directly. Hence the more homogenous HAZ is observed for 6µm/pass and larger.

The observations in *Figs 3.25-7* lend support to the hypothesis that ~5 µm/pass is the optimal depth/pass. Both the 5 and 6 µm/pass scribes were present on the same sample (Sample # 640,1,8), and hence saw identical etching treatments. However, the appearance of the HAZ is very different on each sample. The homogenous HAZ observed on the 6 µm/pass samples and larger increments indicate a smaller amount of debris was ejected from the scribe for the 100 passes made, as was also found in the cut width measurements. This, coupled with the fact that the cut width has been found to be independent of depth/pass, would indicate 5 µm/pass scribe would be deeper as more material was removed. The HAZ can clearly be seen to be less prevalent for the 5 µm/pass sample, so heating effects due to scribing have been minimised, and amount of material removed has been maximised. It is reasonable to assume that 6 µm/pass represents the depth/pass above which the laser beam will be focused continually at a point blow the tip of the trough of the scribe, causing excessive heating and less than optimal amount of material to be removed.

In summary the cut width measurements support the original predictions made – the cut width is independent of the depth-pass when measured directly. There is a peak in the amount of material removed from the scribe and a mimimisation of heating effects at a depth/pass of 5 µm/pass. This may now be taken to be the optimal depth/pass for the scribing of the Genesis collector materials.

3.5 Three-Point Flexure Tests

It was decided that a more quantitative measure of the success or otherwise of the various alterations made to the scribing parameters must be made. A 'successful' scribe would produce an easily cleaved line. A measure of 'ease of cleave' would be the flexural strength of the sample after scribing. In order to test this parameter in a consistent and reliable way, ASTM standard C1161-02c [38] was used in the design of experimental parameters. From this standard the *three-point bend test* was selected due to the small size of the samples making a four-point bending test impractical. The three point bending tests involves the sample being placed horizontally on two supports spaced a set distance apart, (points of contact are freely rotating rollers), and being loaded in compression centrally by a third support.

A *Sintech 20/G* tensile test machine was selected for the tests, using a *10 lb load cell.* The 10 lb cell was selected as it was the most sensitive load cell available for the machine. Its suitability was tested by pressing on the load cell with the same amount of force required to cleave the wafers (judged by touch) and being able to record sufficient variation in output for accurate

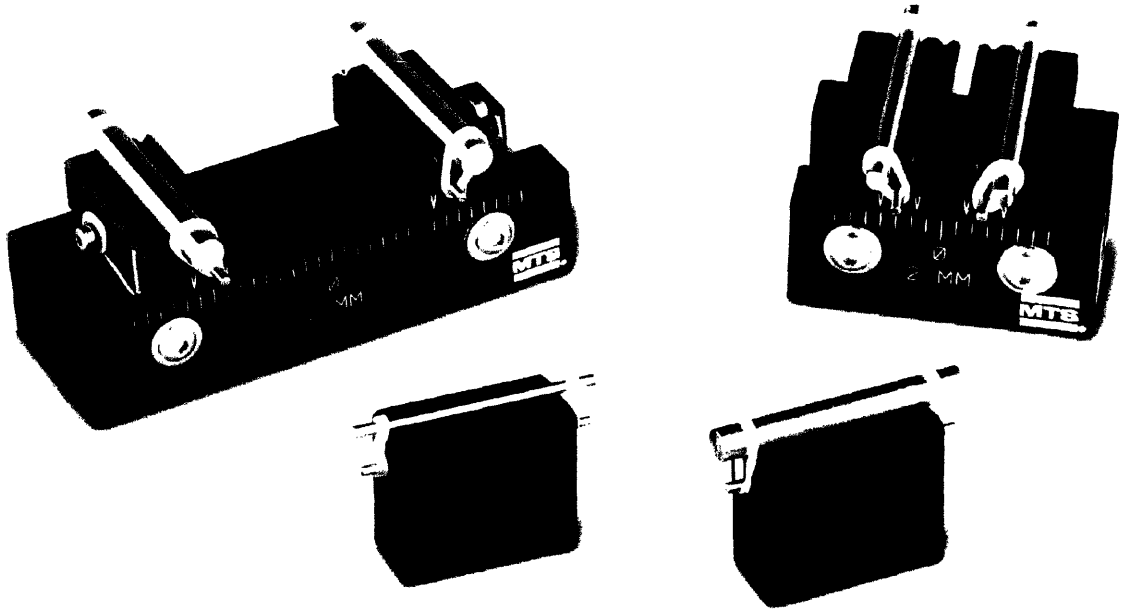

Fig 3.29: MTS 642.001A Bending Fixtures

measurements to be made. However, the bending fixtures (*MTS 642.01A*) were too large to comply with the restrictions of the ASTM standard – The rollers were of too large a diameter for the thickness of specimen under test. MTS does make a set of bending fixtures of the dimensions required (*MTS 642.001A*, as in *Fig 3.29*) – at a cost of $2180. This cost was considered excessive, and modifications were made to the existing bending fixtures to allow the use of smaller diameter rollers. These are illustrated in *Fig 3.30*. The material constraints shown and the dimensions were those specified by the ASTM standard. The standard also specified specimen dimensions, including the thickness of the specimen. The thickness of the wafers was not something we could control, but was considered an acceptable deviation from the standard. The support span suggested by the standard (distance between the two supports) was *40mm. Fig 3.31* shows the specimen dimensions decided upon from the standard.

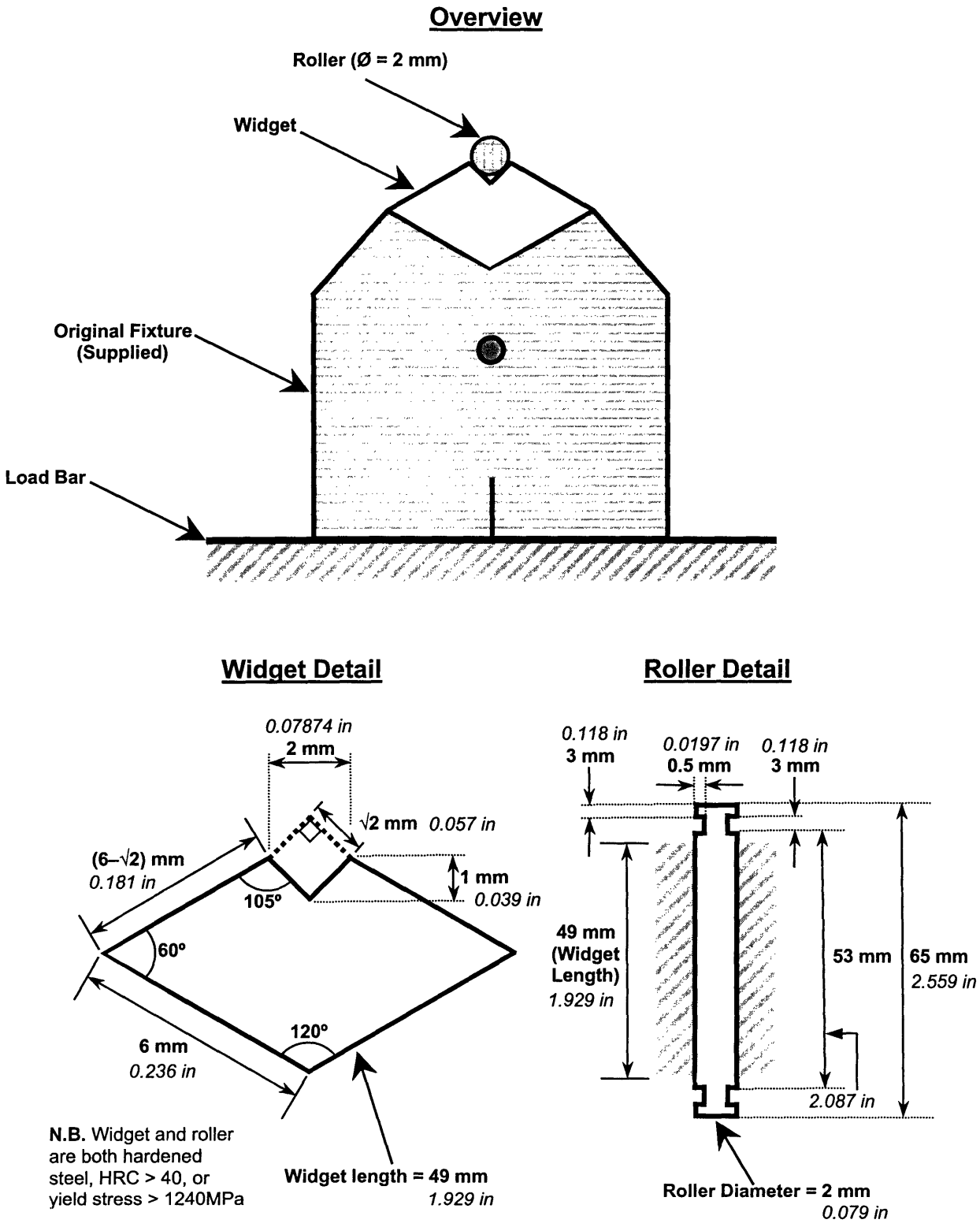

Fig: 3.30 Modifications to MTS 642.01A bending fixture

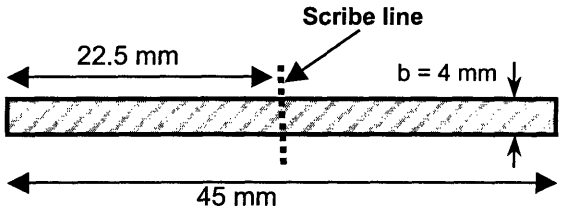

Fig 3.31: Standard Flexural Strength Specimen – Config. B.

It was decided that for each variation of each scribing parameter that there would be a corresponding set of flexural tests to quantify the success of the variation.

The formula used to calculate the flexural strength of the specimens can be seen in *Eqn. 3.2.*

$$S = \frac{3PL}{2bd^2}$$

S = Flexural Modulus (Pa)

P = Breaking Load (N)

L = Support Span (m)

b = Specimen Width (m)

d = Specimen Thickness (m)

Eqn. 3.2: Flexural Strength

The final step in deciding on the feasibility of this as a test method for our samples was to perform a test run. Specimens were prepared with a single scribe line as shown in *Fig 3.23*, one with a cutting speed of *1 mm* s^{-1}, and another with a cutting speed of *15 mm* s^{-1}. Each sample had *100 passes* in total, with a *5 µm/pass* z-axis increment. The loading speed used for the test was *0.05 mm* s^{-1}. The 1 mm s^{-1} sample fractured perfectly along the scribe line, while the 15 mm s^{-1} sample's fracture originated on the scribe line, but then deviated at an ~30° angle from the scribe line. Both fracture surfaces were perpendicular to the surface of the sample. The result of the initial test was that that it was indeed possible to distinguish the flexural modulus of the two specimens: $S_{1mm/s}$ = 62.6 MPa, and $S_{15mm/s}$ = 95.2 MPa. The higher fleuxural modulus of the sample scribed at 15 mm s^{-1} is probably the reason for the deviation form the scribed line – it is likely that the fracture that was initiated along the scribe deviated from that path to follow a crystallographic plane of symmetry – (110) in this case. This highlights the importance of identifying the orientation of each collector array plate prior to scribing. It also suggests that for a sufficiently deep scribe, the symmetry of the Si is unimportant in as far as the fracture will follow the scribe in preference to the (110) plane. However further testing is required to support these conclusions.

Unfortunately, research into using the flexural modulus of each specimen as a method of qualification of success or not of each scribing parameter variation was cut short. This method of testing avoids relying on the accuracy of measurements of cut width and depth by eye. A large number of measurements must be made for each specimen, as detailed in the standard. Making these tests would be a significant undertaking. Given more time in the future this method would be a powerful tool in developing scribing parameters not just for the Genesis collectors, but for the whole silicon scribing industry.

3.6 Heating Effects

The extent to which the laser heats the sample is an important consideration when developing scribing parameters. To that end, it is desirable to assess the extent of the affected zone. *Fig 3.22* shows a zone of material roughly 30μm either side of the scribe line that seems to be affected by the heating. As discussed earlier, the 'haze' is due to the oxidation of the Si by heating effects of the laser. It has been seen that this is not simply as a result of fine debris on the surface, as the haze is still present after cleaning with 30% KOH. The haze is a characteristic feature of all of the SEM observations made of the scribed lines, regardless of scribing parameters.

An important observation made during testing was the formation of cracks running along side the scribed lines. Examples of this phenomenon are shown clearly in *Fig 3.32*.

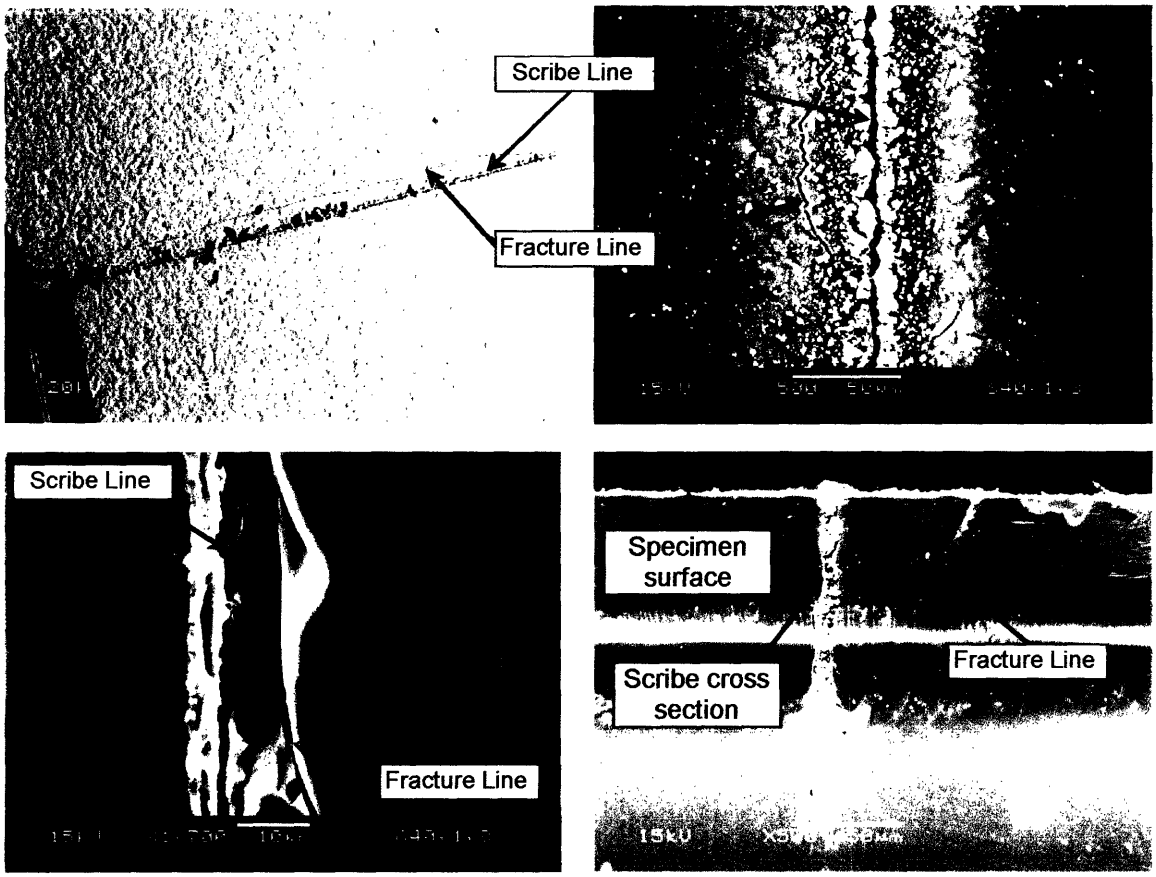

Fig 3.32: SEM Micrographs of thermally induced fractures in the Heat Affected Zone

The fracture lines mostly occur within the extent of the HAZ, leading to the conclusion the cracks are somehow thermally induced. One explanation for this could be heating of the edges of the scribe by the unfocused 'cone' of the laser beam (see *Fig 3.28*) – as the scribe gets deeper, the laser beam (delivered in the form of a focused cone of energy) would ideally follow the new surface at the bottom of the scribe as it was created. In order for the focal point to remain at the bottom of the scribed line, the remainder of the sides of the 'cone' would impinge on the edges of the material as the scribe gets progressively deeper, as is shown in *Fig 3.23*. This is the most likely reason for the formation of the heat affected zone.

The path of the fracture line in the bottom-right figure in *Fig 3.32* adds support to the theory of the cone of focus being the cause of the HAZ. The image is a cross section of a deep scribe into the silicon substrate. The cross-section was prepared by scribing a straight line on the silicon, and cleaving it to produce a straight edge. A second scribe was then performed orthogonal to the prepared edge such that the scribe 'broke through' the edge. The surface was then polished to

remove cutting debris and expose the cross section of the second scribe as shown. *Fig 3.28* suggests the profile of the HAZ would be triangular through the depth of the sample, as would be marked by the path of the fracture shown in *Fig 3.27* (bottom-right). The reason the heating would cause fracture would be thermal shock/relaxation stress relief. Thermal stresses could be induced along the path of the scribe as the laser heats a local area, then moves along the path of the scribe, exposing each unit cross section to a rapid heating and cooling cycle each pass. This would induce thermal cracking.

The observations made of such thermal shock cracking of the samples in the region of the scribed lines suggested that such a phenomenon could be used to an advantage in the form of thermally induced cleavage of the scribed samples. Liquid nitrogen was poured onto the surface of a sample with three scribed lines (scribed @ $1mms^{-1}$, 10µm/pass z-inc., and 60, 80 and 100 passes). Unfortunately the temperature shock had no visible effect on the sample, and no cleavage was observed.

Observation of a larger number of scribe cross-sections would help to quantify the thermal shock theory, but it remains a theory at the time of writing.

A final observation that may be made from the cross-sectional view of the scribe would be the shape of the HAZ around the tip if the scribe line. Much debris is visible in the trough of the scribe. It is possible that the depth of the scribe is too great for the debris to be removed by the vacuum system. The debris collected in the trough of the scribe may act so as to deflect the laser beam to the walls of the scribe, and produce the 'arrow head' HAZ observed at the tip of the scribe. If this is the case, then it is likely that there will be a depth of scribe where this effect causes 100 % attenuation of the laser beam, and no further material may be removed, only the HAZ may grow with each successive scribe after this point. However, a more details study of scribe cross-sections must be made to support this argument.

4.0 Kinetic Modelling of SiO_2 Band Broadening

4.1 Conceptual Description

This section discusses the development of a kinetic model to predict the amount of contamination (in the form of silicon oxide) present on the surface of the silicon collector materials upon their return to Earth. The Si wafer manufacturers, MEMC [26], reported that the native oxide was stripped from the wafers, and a 12Å thick layer of stoichiometric SiO_2 was thermally grown on their surface. This was to suppress the formation of the *native oxide* - a layer of SiO_2 that grows in ambient conditions on the surface of untreated silicon. This oxide grows in unpredictable geometries and thicknesses. The deliberate growth of a thin layer of SiO_2 under controlled oxidation conditions (producing a uniform layer of SiO_2) has been found to be an effective way of suppressing the formation of the native oxide [8-10, 26]. The aim of this model is to predict the extent of modification of the oxide layer caused by exposure to the sun during collection. This is so as to isolate this effect from oxidation caused by radiation exposure and from contamination upon landing. This is important, as the only relevant measurement that may be made on the returned samples is the total oxide thickness due to all possible oxidation sources.

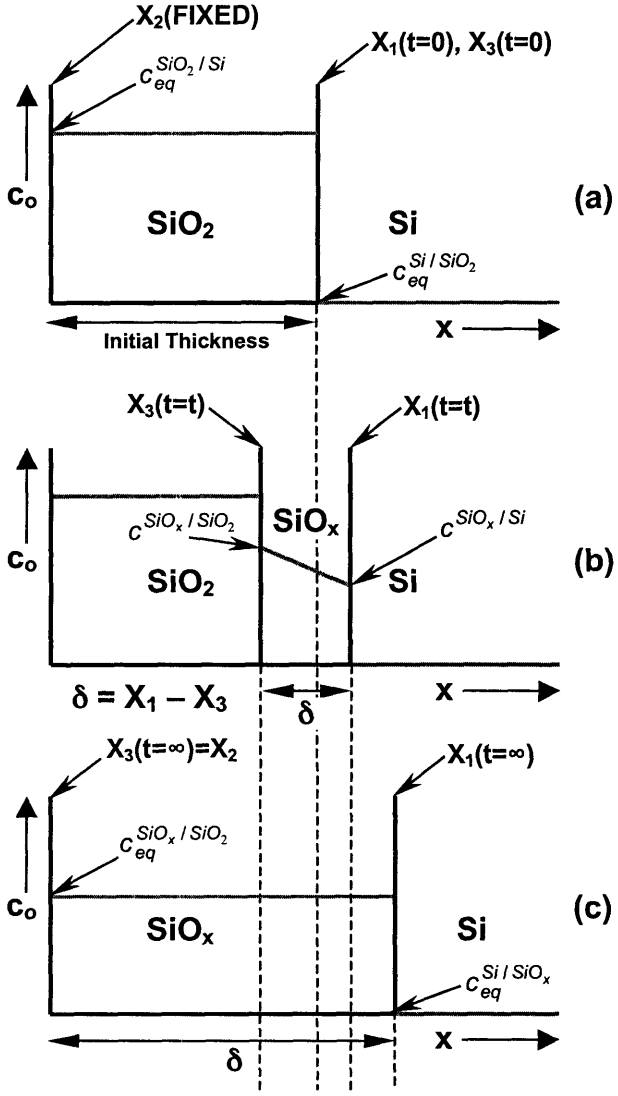

Fig 4.1: Schematic of SiO_2 band broadening at three time intervals: (a) t=0, (b) t=t, (c) t=∞

It is proposed that the existing SiO_2 layer when exposed to an elevated temperature over a long time period will undergo a volume change, known as SiO_2 'band broadening'. At time t=0 (at launch), this has been measured to be 17 Å [2-3]. The 17 Å layer was a result of the original 12 Å layer oxidising further during the pre-flight preparations of the spacecraft (~2.5 years). During this time the wafers were exposed to the atmosphere at room temperature, and a small amount of further oxidation occurred. The 'extra' SiO_2 grown in this way before flight was considered to be fully stoichiometric due to the large timescale allowed for diffusion. The large timescales would allow the exchange reaction of oxygen at the SiO_2 / atmosphere interface to have ceased as the equilibrium concentration of oxygen in the SiO_2 would be reached.

The volume change is brought about by the formation of a less dense *suboxide* SiO_x (where x<2) [26]. The formation of this SiO_x band is summarized in *Fig 4.1*. The grey lines show the relative oxygen concentration; the lines X_1, X_2, and X_3 represent phase boundaries; δ represents the thickness of the growing suboxide layer. The total oxide thickness (δ + the remaining thickness of SiO_2) can be determined by fairly simple deduction. The concentrations are denoted as: $c^{\alpha/\beta}$ – this represents the concentration (in this case oxygen) at the α/β boundary, on the α side. Similarly $c^{\beta/\alpha}$ represents the

concentration of oxygen on the β side of the α/β boundary. It has been suggested in the literature that the oxygen solubility in bulk Si is practically zero [27], and is considered a good approximation for use in this study.

There are a limited number of oxidation states in which Si may exist, as illustrated by *Fig 4.2* [20]. Extensive X-ray photoelectron spectroscopy (XPS) studies have been performed on the Si/SiO_2 system [20] grown under conventional (900°C in dry oxygen for 3 minutes) industrial thermal oxidation procedures. These suggest that suboxide states such as those in the figure are localized near the Si/SiO_2 interface. For (100) oriented Si, it was found that the dominant suboxide species was SiO within roughly 10Å of the Si/SiO_2 interface (as opposed to (111)-oriented Si where Si_2O dominates in this region). The Si_2O_3 suboxide species was found to be present further away from the interface, and was detected up to 30Å into the bulk Si. This suggests that the most likely candidates for SiO_x are SiO, and possibly Si_2O_3. Hence, it is these

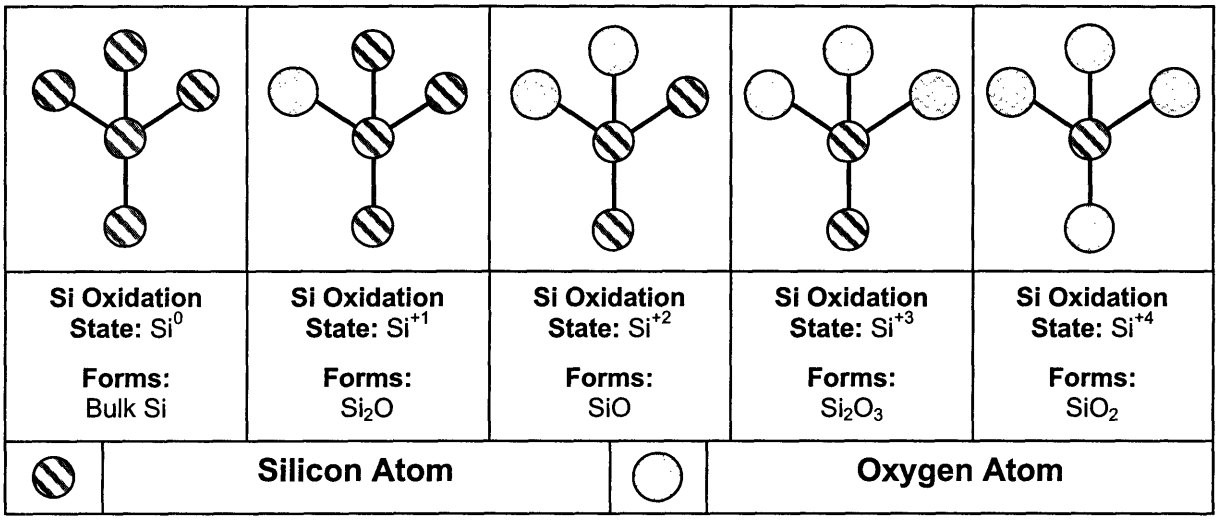

Fig 4.2: Five possible formal oxidation states for silicon.

species that are considered in this derivation.

Initially only the SiO_2 layer is present on the Si substrate. Once in space and exposed to the sun (at T≈165°C [28]), the elevated temperature will allow the oxygen in the SiO_2 to diffuse to the X_1/X_3 boundary. This allows the formation of SiO_x via reactions at the X_1 and X_3 interfaces (for further details refer to *Section 4.2*). As the reactions proceed, some of the bulk Si is transformed into SiO_x, causing the X_1 boundary to move in the positive x direction. Similarly, depletion of the oxygen in the SiO_2 causes the X_3 boundary to move in the negative x direction. The X_3 boundary will eventually (within a very large timescale) move to react with all the available oxygen in the SiO_2 phase, thus completing the 'broadening' process. The time required for 'completion' is unclear at the time of defining the model, and is one question the material may answer. The time the collector arrays are exposed may not be sufficient for the complete conversion to SiO_x.

The concept of the formation of a suboxide layer as an intermediate between the Si and the SiO_2 layer is not a new concept and is well documented in the literature. Hattori et al. [22] found there to be to an intermediate layer of SiO present on the Si surface under conventional thermal oxidation procedures, using XPS measurements. This layer, they suggest, approaches a constant thickness for thin films (such as that present on the Genesis collectors). Raider [23] explicitly identified SiO as being an essential intermediate compound in the oxidation of Si to SiO_2, without which oxidation could not proceed. He also suggested SiO could remain as a stable phase in the Si-O system. Their results also support Grunthaner et al. [20], in that trace amounts of Si_2O_3 were found to be present in the bulk SiO_2 near the interface. Da Silva Jr. et al. in three separate publications [24-26] modelling the early stages of the oxidation of silicon, refer explicitly to a transition layer between the bulk SiO_2 and the Si substrate. They suggest that the layer forms

rapidly in the initial stages of thermal oxidation, and is self-limiting in thickness (~ 30Å). This layer is then said to 'drift' across the silicon bulk, forming SiO_2 behind it. The Genesis collector oxide film is predicted to be < 30Å in thickness. Hence it is proposed that it is a valid hypothesis that oxidation of the Si/SiO_2 system would begin by formation of such a transition layer, which would grow to 'self affine oxidation front' described by da Silva Jr. [26] and may be entirely composed of the transition oxide layer.

4.2 Derivation of Kinetic Model

The first step in defining a model for the system described in *Fig 4.1* is to point out that the broadening of the SiO_x could be *diffusion-* or *reaction-controlled.* That is to say, the rate limiting step (and hence the defining kinetics of the system) could either be the rate at which the diffusants (O and/or Si) reach the interfaces X_1 and X_3 (*diffusion control)*, or the rate at which the interfacial reaction is able to proceed at said interfaces (*reaction control*). The following derivation makes no assumptions as to which is the dominant mechanism.

The following are the possible reactions at the X_1 and X_3 interfaces:

$$X_1: \quad Si + \tfrac{1}{2}O_2 \xrightarrow{k_1} SiO \qquad (Eq.\ 4.1)$$

$$2Si + \tfrac{3}{2}O_2 \xrightarrow{k_1} Si_2O_3 \qquad (Eq.\ 4.2)$$

$$X_3: \quad SiO_2 \xrightarrow{k_3} SiO + \tfrac{1}{2}O_2 \qquad (Eq.\ 4.3)$$

$$2SiO_2 + Si \xrightarrow{k_3} 2Si_2O_3 \qquad (Eq.\ 4.4)$$

The following equations describe the flux of oxygen atoms within the SiO_x layer, across the X_1 and X_3 boundaries:

For the *X_1 boundary* (the Si/SiO_x boundary):

Eq. 4.5 shows that the flux of oxygen across the Si/SiO_x boundary is proportional to the departure from the equilibrium concentration of oxygen at the SiO_x side of the interface. This is the *driving force* for the flux. This is multiplied by a *reaction constant*, K_1 for the reaction (either *Eq. 4.1*, or *Eq. 4.2*).

$$J^{SiO_x} = K_1(c_{eq}^{SiO_x/Si} - c^{SiO_x/Si}) \qquad (Eq.\ 4.5)$$

Eq 4.6 is simply a mass conservation equation. If the X_1 boundary moves a certain amount in time t, then the SiO_x will have to incorporate a certain amount of Si (as the X_1 boundary moves to consume the Si in our case).

$$J^{SiO_x} = \frac{dX_1}{dt}(c^{SiO_x/Si} - c_{eq}^{Si/SiO_x}) \qquad (Eq.\ 4.6)$$

Similar equations for the X_3 boundary may be written:

$$J^{SiO_x} = K_3(c^{SiO_x/SiO_2} - c_{eq}^{SiO_x/SiO_2}) \qquad (Eq.\ 4.7)$$

$$J^{SiO_x} = \frac{dX_3}{dt}(c^{SiO_x/SiO_2} - c_{eq}^{SiO_2/SiO_x}) \qquad (Eq.\ 4.8)$$

In the absence of any data to the contrary, a linear concentration profile for oxygen across the SiO_x layer will be assumed. This is linked to the flux by the following equation:

$$J^{SiO_x} = -\tilde{D}^{SiO_x}\frac{(c^{SiO_x/SiO_2} - c^{SiO_x/Si})}{X_3 - X_1} \qquad (Eq.\ 4.9)$$

The first term in *Eq. 4.9* is the *interdiffusivity* in SiO_x. This is defined as:

$$\tilde{D}^{SiO_x} = (c_O^{SiO_2/Si} \cdot \Omega_O^{SiO_2} \cdot D_{Si}^{SiO_2}) + (c_{Si}^{SiO_2/Si} \cdot \Omega_{Si}^{SiO_2} \cdot D_O^{SiO_2})$$

Where:

$\Omega_O^{SiO_2}$ = Atomic volume of O in SiO_2

$\Omega_{Si}^{SiO_2}$ = Atomic volume of Si in SiO_2 *(Eq. 4.10)*

$D_{Si}^{SiO_2}$ = Intrinsic diffusivity of Si in SiO_2

$D_O^{SiO_2}$ = Intrinsic diffusivity of O in SiO_2

The intrinsic diffusivities are expected to follow an Arrhenius relationship with temperature.

N.B. The equations *Eq. 4.5* and *Eq. 4.7* show that $c^{SiO_x/Si} \leq c_{eq}^{SiO_x/Si}$ and $c^{SiO_x/SiO_2} \geq c_{eq}^{SiO_x/SiO_2}$ since J^{SiO_x} is in the positive x-direction (see *Fig 4.1*), and the fact that rate constants are positive.

Equating *Eq. 4.5* and *Eq. 4.6*:

$$(c_{eq}^{SiO_x/Si} - c^{SiO_x/Si}) = \frac{\tilde{D}^{SiO_x}}{(X_3 - X_1)K_1}(c^{SiO_x/Si} - c^{SiO_x/SiO_2}) \qquad (Eq.\ 4.11)$$

Equating *Eq. 4.8* and *Eq. 4.9*:

$$(c^{SiO_x/SiO_2} - c_{eq}^{SiO_x/SiO_2}) = \frac{\tilde{D}^{SiO_x}}{(X_3 - X_1)K_3}(c^{SiO_x/Si} - c^{SiO_x/SiO_2}) \qquad (Eq.\ 4.12)$$

To catagorise important regions of behaviour it is useful to group certain constants from the above equations (Eq. 4.11 and 4.12) to define Φ_1 and Φ_2 as follows [29]:

$$(c_{eq}^{SiO_x/Si} - c^{SiO_x/Si}) = \Phi_1(c^{SiO_x/Si} - c^{SiO_x/SiO_2}) \qquad (Eq.\ 4.13)$$

$$(c^{SiO_x/SiO_2} - c_{eq}^{SiO_x/SiO_2}) = \Phi_2(c^{SiO_x/Si} - c^{SiO_x/SiO_2}) \qquad (Eq.\ 4.14)$$

The definitions of Φ_1 and Φ_2 permit certain simplifying approximations to be made:

$\Phi_1(SMALL) \Leftrightarrow c^{SiO_x/Si} \cong c_{eq}^{SiO_x/Si}$

$\Phi_1(LARGE) \Leftrightarrow c^{SiO_x/Si} \cong c^{SiO_x/SiO_2}$

$\Phi_2(SMALL) \Leftrightarrow c^{SiO_x/SiO_2} \cong c_{eq}^{SiO_x/SiO_2}$

$\Phi_2(LARGE) \Leftrightarrow c^{SiO_x/Si} \cong c^{SiO_x/SiO_2}$

The relative magnitudes of these constants allow the limiting kinetic regimes for the system to be identified:

- Φ_1 & Φ_2 *LARGE – Reaction Control*: This implies that there is a large build up of oxygen at the interfaces (thus a small value of flux), causing a large departure from the equilibrium oxygen concentration at the interface. The rate limiting step is the rate of the interfacial reactions.
- Φ_1 & Φ_2 *SMALL – Diffusion Control*: The concentration of oxygen at the interface is close to the equilibrium concentration of oxygen in each phase on either side of the interface. This implies that the reaction rate at the interface matches or exceeds the rate of oxygen delivery. The rate limiting step is the diffusive transport of the oxygen to the interfaces.

- Φ_1 & Φ_2 *MIXED MAGNITUDE – Mixed Kinetics*: There is no clear dominant kinetic mechanism.

Mixed kinetics may occur in a system such as this when the SiO_x layer grows beyond a critical thickness, then the kinetics may change from being reaction dependent (as would be expected for very thin films) to being diffusion dependent. When the SiO_x layer is very thin, then the diffusion path for the oxygen would be very short, hence the growth of the SiO_x layer would be controlled by the reaction rates at the interfaces. As the SiO_x layer grows the diffusion path gets larger, and the diffusion rate of the oxygen through the SiO_x becomes more of a controlling factor than the interfacial reaction rates, and the kinetics switch from being reaction controlled to being diffusion controlled. In between these limiting cases lies the region of *mixed kinetics.*

Using the approximations above for diffusion and reaction control it is possible to develop growth relations for the thickness of the SiO_x layer. This thickness X is defined as the distance between the X_1 and X_3 boundaries: $X = X_3 - X_1$.

For *diffusion control*, $c^{SiO_x/Si} \cong c_{eq}^{SiO_x/Si}$, and $c^{SiO_x/SiO_2} \cong c_{eq}^{SiO_x/SiO_2}$. This corresponds to a large (steep) gradient in the concentration profile of oxygen in the SiO_x layer. Substituting this into Eqs. 4.6, 4.8, and 4.9:

$$\frac{dX_1}{dt} = \frac{J^{SiO_x}}{(c_{eq}^{SiO_x/Si} - c_{eq}^{Si/SiO_x})}$$

$$\frac{dX_3}{dt} = \frac{J^{SiO_x}}{(c_{eq}^{SiO_x/SiO_2} - c_{eq}^{SiO_2/SiO_x})}$$

$$\frac{d(X_3 - X_1)}{dt} = -\tilde{D}^{SiO_x} \frac{(c_{eq}^{SiO_x/SiO_2} - c_{eq}^{SiO_x/Si})}{X_3 - X_1} \left[\frac{1}{(c_{eq}^{SiO_x/SiO_2} - c_{eq}^{SiO_2/SiO_x})} - \frac{1}{(c_{eq}^{SiO_x/Si} - c_{eq}^{Si/SiO_x})} \right]$$

$$X \frac{dX}{dt} = -\tilde{D}^{SiO_x} (c_{eq}^{SiO_x/SiO_2} - c_{eq}^{SiO_x/Si}) \left[\frac{1}{(c_{eq}^{SiO_x/SiO_2} - c_{eq}^{SiO_2/SiO_x})} - \frac{1}{(c_{eq}^{SiO_x/Si} - c_{eq}^{Si/SiO_x})} \right] \quad \text{(Eq. 4.15)}$$

Equation *Eq. 4.15* predicts a *parabolic growth for diffusion control.*

For *reaction control*, $c^{SiO_x/Si} \cong c^{SiO_x/SiO_2} \cong \bar{c}$. This corresponds to an almost flat concentration gradient of oxygen in the SiO_x layer. Thus an average oxygen concentration $\bar{c}$ may be defined for this layer in terms of the reaction constants K_1 and K_3 using *Eq. 4.5* and *Eq. 4.7*:

$$J^{SiO_x} = K_1(c_{eq}^{SiO_x/Si} - \bar{c})$$

$$J^{SiO_x} = K_3(\bar{c} - c_{eq}^{SiO_x/SiO_2})$$

$$\bar{c} = \frac{K_1 c_{eq}^{SiO_x/Si} + K_3 c_{eq}^{SiO_x/SiO_2}}{K_1 + K_3} \quad \textit{(Eq. 4.16)}$$

However, for our case, the stoichiometry of the SiO layer will fix the value for the average oxygen concentration. Simple calculation using the literature density value for SiO and the atomic mass of oxygen yields a value for $\bar{c} = 0.136$ mol cm^{-3}.

Equating *Eq. 4.5* and *Eq. 4.6*, and using the average concentration:

$$K_1(c_{eq}^{SiO_x/Si} - \bar{c}) = \frac{dX_1}{dt}(\bar{c} - c_{eq}^{Si/SiO_x})$$

$$\frac{dX_1}{dt} = K_1 \frac{(c_{eq}^{SiO_x/Si} - \bar{c})}{(\bar{c} - c_{eq}^{Si/SiO_x})} \qquad (Eq.\ 4.17)$$

Similarly for *Eq. 4.7* and *Eq. 4.8:*

$$\frac{dX_3}{dt} = K_3 \frac{(\bar{c} - c_{eq}^{SiO_x/SiO_2})}{(\bar{c} - c_{eq}^{SiO_2/SiO_x})} \qquad (Eq.\ 4.18)$$

Thus to get the growth rate for *reaction control* the difference of *Eq. 4.18* and *Eq. 4.17* must be taken:

$$\frac{d(X_3 - X_1)}{dt} = \frac{dX}{dt} = K_3 \left[\frac{(\bar{c} - c_{eq}^{SiO_x/SiO_2})}{(\bar{c} - c_{eq}^{SiO_2/SiO_x})}\right] - K_1 \left[\frac{(c_{eq}^{SiO_x/Si} - \bar{c})}{(\bar{c} - c_{eq}^{Si/SiO_x})}\right]$$

$$\underline{\underline{\frac{dX}{dt} = K_1 \left[\frac{(\bar{c} - c_{eq}^{SiO_x/Si})}{(\bar{c} - c_{eq}^{Si/SiO_x})}\right] + K_3 \left[\frac{(\bar{c} - c_{eq}^{SiO_x/SiO_2})}{(\bar{c} - c_{eq}^{SiO_2/SiO_x})}\right]}} \qquad (Eq.\ 4.19)$$

Equation *Eq. 4.19* predicts a *constant growth rate for reaction control.*

The separation of oxidation regimes into linear and parabolic laws was also found in the original oxidation studies performed by Deal and Grove [11] and many subsequent studies [4,5, 13-18, 24-26]. [24] suggests the initial growth phase of the film proceeds by a parabolic growth of the 'oxidation front' with time. This refers to the transition layer discussed in the literature, which is most likely a suboxide. The implication of the literature results to this model would be that the initial growth of the SiO_x layer is governed by the parabolic rate law (*Eq. 4.15*), and if the film were to grow into the thick regime (>30 Å), then kinetics might best be described by the linear growth law (*Eq. 4.19*). This is counter to the expected behaviour described on the previous page. It is precisely this kind of counter-intuitive behaviour that is the cause of the controversial disagreements over the mechanism of SiO_2 thin film growth in the literature.

4.3 Application of Kinetic Model

The above model potentially can predict the oxide thickness on the surface of the silicon collector materials when they return to Earth. The equations show an explicit dependence on time, and an implicit dependence on temperature – both the reaction constants and the interdiffusivity values have an Arrhenius relationship with temperature and finite activation energy for the process. However, the constants and concentrations used in the model must be evaluated in order to use the model.

The Si^{2+} oxidation state has been found, through extensive XPS studies, to be the dominant oxidation state at the silicon-oxide interface for (100) oriented Si [13]. Thus SiO_x can be taken to be SiO (x=1), allowing the calculation of some of the unknown variables in the models above.

The most obvious of the constants to find is the concentration of oxygen in the silicon, on the silicon side of the X_1 boundary, namely $c_{eq}^{Si/SiO}$. This is defined in the initial description of the model to be equal to zero, due to the extremely low solubility of oxygen in bulk silicon.

Next, the equilibrium concentration of oxygen in SiO_2 is a relatively simple calculation. The literature density of SiO_2 is given as $2.196\ gcm^{-3}$, and the atomic mass of oxygen is given as $15.9994\ gmol^{-1}$. Thus the atomic volume of oxygen in SiO_2 may be calculated, as shown in *Eq. 4.20.*

$$\Omega_O^{SiO_2} = \frac{Mass(O)}{Density(SiO_2)} = \frac{15.9994}{2.196} = 7.286\ cm^3 mol^{-1}$$
$$\Leftrightarrow c_{eq}^{SiO_2/SiO} = \frac{1}{\Omega_O^{SiO_2}} = \underline{\underline{0.137\ mol\ cm^{-3}}} \qquad (Eq.\ 4.20)$$

The effective diffusivity, or interdiffusivity, has been found experimentally by Whidden et al. [6,7] as a function of temperature, as shown in *Eq. 4.21.*

$$\tilde{D}^{SiO} = (1.68 \times 10^{13}\ m^2 h^{-1}) \exp\left[\frac{-2.65 eV}{k_B T}\right]$$

k_B = Boltzmann constant (eV K^{-1}) (*Eq. 4.21*)

T = Temperature (K)

To find the reaction constants K_1 and K_3, attention was directed towards various kinetic resources in the current literature [30-32]. Unfortunately it was found that the formation of SiO from its constituent elements was not a well understood reaction. Consequently the values for the reaction constants associated with *Eq. 4.1* and *Eq. 4.3* are not known. Experimental determination of rate constants would be a very involved process. It would involve the real-time measurement of the evolution of the reaction products. This was done by Yu and Eldridge [33], who studied in real time the oxidation of Si (100) in air at elevated temperatures (700 – 950 °C) through the use of controlled pulses of oxygen and time-resolved mass spectroscopy. They were able to observe the formation of the SiO as an intermediate step towards forming SiO_2 (Langmuir kinetics [6,7]), and measured an overall reaction constant as a function of temperature for the formation of SiO_2. However, their results were not directly comparable to the Genesis model, as the reactions in *Section 4.2* occur in the solid state with a fixed oxygen supply at a temperature far lower than that used by Yu and Eldridge. The reaction would progress at a much reduced rate, possibly not yielding a detectable amount of reaction product in a suitable time frame. Another approach could be to measure the evolution of the reaction products by the use of a radioactive or chemical tracer such as O^{19} (decays to F^{19}, easily detectable as F contamination is not likely to be significant in laboratory conditions) [42]. Such studies are beyond the scope of this thesis.

The same level of experimentation must be performed in order to determine the equilibrium concentrations of oxygen within the SiO layer at each of the reaction interfaces, namely $c_{eq}^{SiO/Si}$ and c_{eq}^{SiO/SiO_2}.

To conclude, the kinetic model outlined in the previous section would theoretically be suitable to model the growth kinetics of a suboxide within the SiO_2 layer during flight. However, a great deal of original experimentation must be performed to determine the necessary constants.

A new approach to the modelling must be taken so as to reduce the number of unknown/undeterminable variables.

4.4 Reduction of Number of Unknown Variables

There exist in the literature many models for the oxidation of silicon *in air* [4,5, 13-18, 24-26]. Most of these models deal with very *high temperature* oxidation and/or *thick (>200 μm) oxides.* They are obviously not directly applicable to the conditions in the Genesis model. However, a new approach for modelling the Genesis condition might be to use some of the basic derivation steps used in the classical Deal-Grove paper [11], in combination with those used by Whidden et al. [6,7]. The model proposed by Whidden et al. is derived from a similar reaction scheme as was proposed in *Section 4.1*, in that SiO is formed as the first reaction product, and then further oxidation yields the SiO_2. The Whidden model has a distinct advantage over that developed so far for the Genesis mission in that there are seemingly far fewer unknown variables. The final model uses only a single reaction constant, an equilibrium concentration of oxygen within SiO, the number of oxygen molecules per unit volume of oxide, and an experimentally determined

Table 4.1: Comparison of Deal-Grove and Genesis kinetic models

Whidden et al. Model	Genesis Model
Models growth of SiO_2 layer using oxygen from the atmosphere as the oxidant source. This is an *infinite source of oxygen.*	Models SiO growth using the oxygen within SiO_2 as the oxidant source. This is a *finite source of oxygen.*
Oxygen is first adsorbed at the oxide surface (SiO_2) after being transported through the atmosphere: $F_1 = h(c^* - c_o)$ F_1 = Flux h = Gas transport coefficient c^* = Eqm. concentration of O in SiO_2 c_o = Concentration of O at the outer surface of the SiO_2	Oxygen at the inner surface of the SiO_2 layer dissociates from the SiO_2 and forms SiO: $J_1^{SiO} = k_3(c^{SiO/SiO_2} - c_{eq}^{SiO/SiO_2})$ *(Eq 4.7)*
Oxygen is transported across the SiO_2 film to the Si: $F_1 = D_{eff}\frac{(c_o - c_i)}{x}$ D_{eff} = Effective Diffusivity c_i = Concentration of O within SiO_2 at the Si/SiO_2 interface x = Oxide Thickness	Oxygen is transported across the SiO film to the Si: $J_2^{SiO} = -\tilde{D}^{SiO}\frac{(c^{SiO/SiO_2} - c^{SiO/Si})}{(X_3 - X_1)}$ *(Eq. 4.9)*
Steady state assumed in the system – all fluxes are equal.	
Oxygen is reacted at the Si surface to form a new layer of SiO_2. This flux is assumed to be a *first-order chemical reaction*: $F_3 = kc_i$	Oxygen is reacted at the Si surface to form a new layer of SiO: $J_3^{SiO} = K_1(c_{eq}^{SiO_x/Si} - c^{SiO_x/Si})$ *(Eq 4.5)*

The basic concepts of each of the models are summarised below:

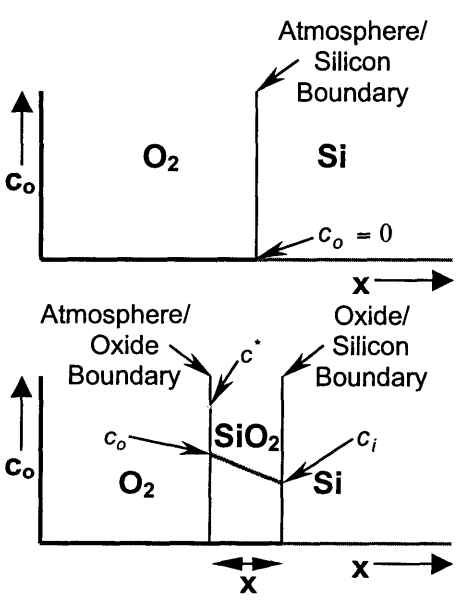

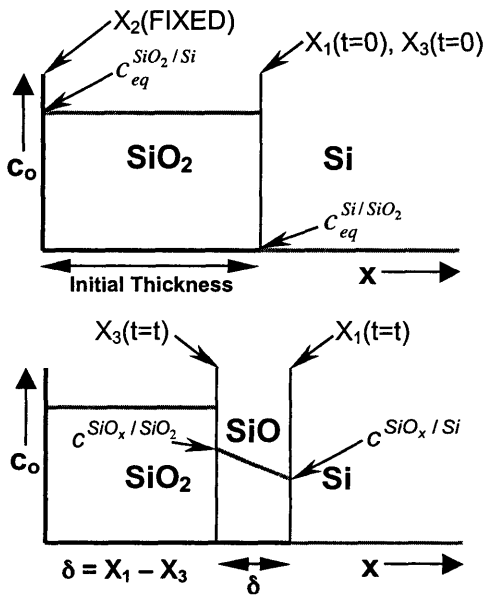

fitting parameter. It is proposed that the number of unknown variables in *Eq. 4.15* and *Eq. 4.19* may be significantly reduced, and may allow this modified version to be applied to the Genesis situation by taking the fluxes for oxygen across the X_1 and X_3 boundaries and substituting them into the Whidden model. *Table 4.1* presents a brief comparison between the Whidden model and the Genesis situation.

A limitation of the Deal-Grove model is that it fails to predict the growth rates of thin films (<200 μm) [4,5, 13-18, 24-26]. One reason for this is that it does into take into account that oxygen availability at the interfaces will vary within the reaction time frame due to diffusional limitations [7]. In terms of the equilibrium reaction, the SiO is simply an intermediate reaction product. The concentration of SiO reaches a constant value after the formation of a sufficiently thick oxide layer on the Si. The Deal Grove model does not take into account the variation in concentration of the SiO in the initial stages of growth, and therefore does not predict thin film growth correctly. Whidden et al. developed such a model for the oxidation of silicon in air starting with the simple Deal-Grove fluxes. It is proposed that the Whidden et al. model be used as a basis for a new model for the Genesis oxidation.

The first step is to use the steady-state approximation and equate all of the diffusive fluxes:

$$J_3 = k_1(c_{eq}^{SiO/Si} - c^{SiO/Si})$$

$$J_2 = \frac{\tilde{D}^{SiO}(c^{SiO/Si} - c^{SiO/SiO_2})}{\delta}$$

$$J_1 = k_3(c^{SiO/SiO_2} - c_{eq}^{SiO/SiO_2})$$

Now setting $J_1 = J_2$ and $J_2 = J_3$:

$$k_1(c_{eq}^{SiO/Si} - c^{SiO/Si}) = \frac{\tilde{D}^{SiO}(c^{SiO/Si} - c^{SiO/SiO_2})}{\delta} = k_3(c^{SiO/SiO_2} - c_{eq}^{SiO/SiO_2})$$

$$\Leftrightarrow c^{SiO/SiO_2} = \frac{c_{eq}^{SiO/Si}\tilde{D}^{SiO}k_1 + c_{eq}^{SiO/SiO_2}(\tilde{D}^{SiO} + \delta k_1)k_3}{\delta k_1 k_3 + \tilde{D}^{SiO}(k_1 + k_3)} \quad \text{(Eq. 4.22)}$$

$$\Leftrightarrow c^{SiO/Si} = \frac{c_{eq}^{SiO/SiO_2}\tilde{D}^{SiO}k_3 + c_{eq}^{SiO/Si}k_1(\tilde{D}^{SiO} + \delta k_3)}{\delta k_1 k_3 + \tilde{D}^{SiO}(k_1 + k_3)} \quad \text{(Eq. 4.23)}$$

The motivation for finding the oxygen concentrations on the SiO sides of the interfaces in terms of calculable quantities is that it is precisely these concentrations that are varying throughout the oxidation process, and they cannot be experimentally determined.

Eq. 4.22 and *Eq. 4.23* are the equivalents of the expressions for c_i and c_o in Whidden et al. and Deal-Grove papers [6, 7, 11]:

$$c_i = \frac{hD_{eff}c^*}{hkx + hD_{eff} + kD_{eff}} \quad \text{(Eq. 4.24)}$$

$$c_o = \frac{h(kx + D_{eff})c^*}{hkx + hD_{eff} + kD_{eff}} \quad \text{(Eq. 4.25)}$$

The main difference with our model is that the equilibrium concentration of oxygen in the SiO is different at each of the interfaces, reflecting the range of non-stoichiometry in SiO. This is illustrated in Fig 4.3, which shows a schematic phase diagram for the silicon-rich end of the Si-O phase diagram. A suitable calculated or experimentally determined phase diagram for this end of the system was not available in the literature [27]. Note the diagram shows a finite, but very small amount of oxygen solubility in silicon. This solubility has been considered so small so as to be

negligible for the purposes of this model [27], as laid out in the previous section. It can be seen that SiO exists over a range of compositions, and that $c_{eq}^{Si/SiO} \neq c_{eq}^{SiO/SiO_2}$.

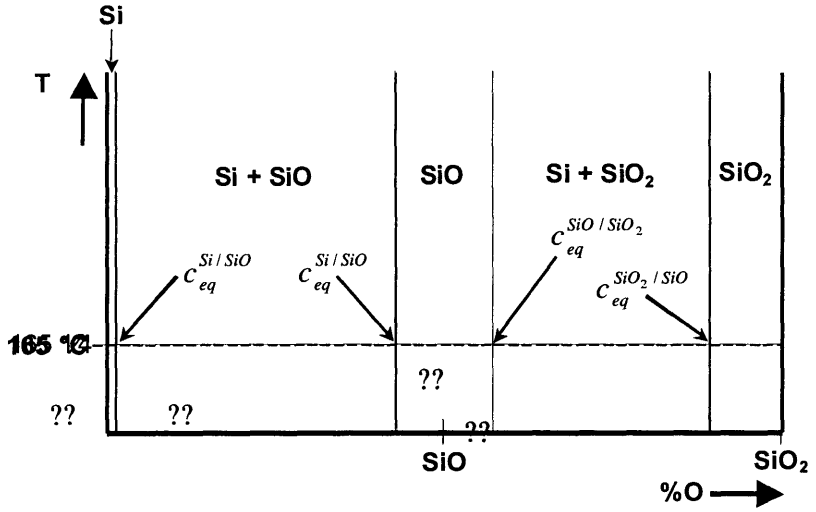

Fig 4.3: Schematic Si-O Phase Daigram

The next simplification Whidden makes is to eliminate *h* from *Eq. 4.24* and *Eq. 4.25*. The approximation that is made is that Whidden suggests that the gas transport coefficient, *h*, is of a much greater magnitude than the reaction constant *k*. He then divides the numerator and denominator of *Eq. 4.24* and *Eq. 4.25* by *h*, thus removing it from the equations. This is equivalent to removing k_1 from *Eq. 4.22* and *Eq. 4.23* by making the approximation that $k_1 >> k_3$. It is proposed that one can make the assumption that the reaction constant $k_1 >> k_3$ on the basis that the *equilibrium constants of formation* (denoted K_{f1} and K_{f3} respectively) that measure the thermodynamic propensity for reaction (ignoring kinetic factors) are in such proportions. K_f is related to the standard free energy change associated with a reaction (_G⁻) which is the difference between the standard free energies of the products and the reactants thus:

$$\ln K_f = -\frac{\Delta G_m^{\Theta}}{k_B T} = -\frac{\Delta H_m^{\Theta}}{k_B T} + \frac{\Delta S_m^{\Theta}}{k_B}$$

Where:

ΔH_m^{Θ} = molar standard enthalpy of reaction

ΔS_m^{Θ} = molar standard entropy of reaction

In the absence of being able to measure or calculate k_1 or k_3 directly, K_{1f} and K_{3f} are tabulated in logarithmic form for a range of temperatures and are readily available for most compounds. The K_f values for elements may be combined to predict the thermodynamic propensity for any given reaction. This is shown for the reactions at the X_1 and X_3 boundaries in *Eq. 4.26*.

$$\begin{aligned} &Si + \tfrac{1}{2}O_2 \xrightarrow{k_1} SiO \\ &\log K_{f1} = \log K_f(SiO) - \log K_f(Si) - \log K_f(O) \\ &SiO_2 \xrightarrow{k_3} SiO + \tfrac{1}{2}O_2 \\ &\log K_{f3} = \log K_f(SiO) + \log K_f(O) - \log K_f(SiO_2) \end{aligned} \qquad \text{(Eq. 4.26)}$$

The *log* K_f values for the elements are zero by definition [30]. Three sources of thermodynamic data were used in the calculation of K_{f1} and K_{f3}, where the mean values for *log* K_f *(SiO)* and *log* k_f *(*SiO_2*)* have been used in calculation [30-32]. The results are shown in *Eq. 4.27*. Note that the

tabulated values are tabulated in steps of 100K, thus the K_f values sown are for 400K or 127°C, and that equilibrium constants are dimensionless [30-32].

$$\log K_{f1} = \log K_f(SiO) - \log K_f(Si) - \log K_f(O)$$
$$\log K_{f1} = 15.122 - 0 - 0$$
$$K_{f1} = 5.71 \times 10^{17}$$
$$\log K_{f3} = \log K_f(SiO) + \log K_f(O) - \log K_f(SiO_2) \qquad \text{(Eq. 4.27)}$$
$$\log K_{f3} = 15.122 + 0 - 108.731$$
$$K_{f3} = 1.06 \times 10^{-91}$$

It is clear that $K_{f1} >> K_{f3}$, and hence the same is assumed for k_1 and k_3. The value for the equilibrium constant K_{f3} reflects the high stability of SiO_2. However, the stability of SiO as a separate phase in the Si-O system is supported by Raider [23].

Raider [23] and Gulbransen [34] suggest that the oxidation process proceeds by the formation of a reaction intermediate SiO*, which may take on more oxygen to become SiO_2, but may also be converted to stable SiO at the interface. Gulbransen showed experimentally that SiO is formed preferentially to SiO_2 at low pressures. The rate at which SiO* is converted to SiO_2 is far slower than the rate at which SiO* is converted to SiO_2 [34]. Thus the rate of formation of SiO from oxygen and silicon (*Eq. 4.1* governed by k_1) is larger than the rate required to convert SiO to SiO_2 (the reverse *Eq. 4.3*). This reinforces that k_1 is large, and k_3 is likely to be small in comparison as SiO_2 is considered the stable oxidation state of Si. Hence $k_1 >> k_3$.

Making the substitution into *Eq. 4.22* and *Eq. 4.23* that $k_1 >> k_3$ yields:

$$c^{SiO/SiO_2} = \frac{c_{eq}^{SiO/Si}\tilde{D}^{SiO} + \delta k_3 c_{eq}^{SiO/SiO_2}}{\delta k_3 + \tilde{D}^{SiO}} \equiv c_i \qquad \text{(Eq. 4.28)}$$

$$c^{SiO/Si} = \frac{\tilde{D}^{SiO} c_{eq}^{SiO/Si} + \delta k_3 c_{eq}^{SiO/Si}}{\delta k_3 + \tilde{D}^{SiO}} = c_{eq}^{SiO/Si} \equiv c_o \qquad \text{(Eq. 4.29)}$$

These equations suggest that $c^{SiO/SiO_2} \equiv c_i$ and $c^{SiO/Si} \equiv c_o$ from the Deal-Grove and Whidden derivations. This would make sense, as c_i is associated with the slower reaction - that of the formation of SiO_2 at the Si/SiO_2 boundary, where the rate is controlled by k_3, which is much smaller than h. c^{SiO/SiO_2} is also associated with the least thermodynamically favourable reaction, as shown in *Eq. 4.27*. Similar comparisons may be made for c_o and $c^{SiO/Si}$.

By performing the substitutions to obtain *Eq. 4.28* and *Eq. 4.29* k_1 has been eliminated, reducing the number of unknown variables by one. $\tilde{D}^{SiO}$ has been experimentally determined as detailed in *Eq. 4.21*, and δ is the quantity of interest.

The final step in developing a model for the oxide growth would be to relate the interfacial oxygen concentrations to a change of oxide thickness δ with time. Using a similar approach to that employed by Whidden [6,7]:

$$\frac{\partial [SiO]}{\partial t} = N\frac{\partial \delta}{\partial t} = k_3 c^{SiO/SiO_2} + \alpha c^{SiO/Si} e^{-\frac{\delta}{a}}$$

$$\frac{\partial \delta}{\partial t} = \frac{k_3(c_{eq}^{SiO/Si}\tilde{D}^{SiO} + \delta k_3 c_{eq}^{SiO/SiO_2})}{N(\delta k_3 + \tilde{D}^{SiO})} + \frac{\alpha c_{eq}^{SiO/Si} e^{-\frac{\delta}{a}}}{N} \qquad \text{(Eq 4.30)}$$

Where :

$[SiO]$ = concentration of SiO

N = number of oxygen molecule per unit volume SiO

a, α = experimentally determined constants.

The exponential factor in *Eq. 4.30* represents a constant of integration introduced to take into account the variation of oxygen availability throughout the time of the reaction at the Si/SiO interface to ensure this model is valid in the thin film regime. The constant α groups together constants such as the silicon concentration (amount of silicon available is assumed constant due to the 'infinite source' compared to oxygen availability), and the rates of reaction (both forward and reverse reactions) associated with *Eq. 4.1* and *Eq. 4.3*. The constant *a* represents a characteristic length within the system. It was suggested by Whidden that *a* represents the thickness of oxide that marks the change from *diffusion-controlled* to *reaction-controlled* kinetics.

Whidden et al. were able to find values for *a* and α by fitting the model to the extensive amount of experimental data available for the oxidation of silicon in air at relatively hightemperatures. A suitable value for α was found to be 4.0×10^6 *μm/min* while the values for a fell in the range *0.28 – 1.0 nm* over a temperature range of 800 –1000 °C. These values are not applicable to the Genesis conditions. However, *Eq. 4.30* would become a viable model if controlled experimentation of silicon oxidation in vacuum were to be performed, and the resulting oxide thicknesses measured. The relationship between the total oxide thickness (SiO_2 + SiO) and the SiO thickness is simple to determine, and is done in *Section 4.5*. This would allow suitable values for *a* and α to be determined for the oxidation of silicon in vacuum at low temperatures. Unfortunately such experimentation has not yet been performed, and is beyond the scope of this thesis.

To conclude, the both of the kinetic models proposed in this chapter could potentially model and predict the thickness of the oxide layer present on the surface of the silicon collector arrays. The development of *Eq. 4.30*, was able to reduce the number of unknown variables associated in predicting the oxide thickness. However, further precise experimentation must be performed in order to determine the remaining unknown constants in the absence of any data in the literature.

4.5 Estimation of Maximum Suboxide Thickness

Section 4.2 suggests that the most likely oxidation state for Si within the suboxide would be Si^{+2}, making the suboxide SiO. SiO has a lower density than SiO_2, and its formation from a fixed mass of SiO_2 would therefore cause an overall volume increase. Since the area of the collector plates are fixed (and hence the area of the oxide film is also fixed) any volume change would manifest as a change in film thickness, as the other two dimensions possible for expansion/contraction are constrained. From these facts, the measured pre-light oxide thickness of 17Å, and the literature densities for SiO and SiO_2, the maximum thickness of a suboxide film of SiO may be calculated. This calculation assumes that elastic constraints within the system do not affect the volume changes proposed.

- The density of SiO_2 is 2.196 g cm^{-3}. Thus for a thickness of 17Å, the mass of SiO_2 per unit area of collector (A) may be calculated:

$$\rho_{SiO_2} = \frac{m_{SiO_2}}{v_{SiO_2}} = \frac{m_{SiO_2}\ \text{g}}{\left(17\times10^{-8}\right)\text{cm}\times A\ \text{cm}^2}$$

$$m_{SiO_2} = 2.196 * (17\times10^{-8} A) = \underline{\underline{3.733\times10^{-7} A\ \text{g}}}$$

- SiO_2 is 46.7 wt.% Si, and 53.3 wt.% O. For the *maximum* thickness of oxide to be formed, assuming the final oxide formed is entirely SiO, then the maximum thickness would be achieved by 100% transformation of the original SiO_2 layer to SiO. The amount of Si present in the oxide would then have to double (one oxygen freed by every SiO_2 molecule being converted to SiO + O). The source of the extra Si is the Si substrate. The Si substrate may be treated as an effectively infinite source of Si (thickness of the substrate is on the order of 600 to 700 μm, in contrast to the Å's of oxide present). Thus the maximum mass of SiO that may be formed is:

  Mass of SiO Film = [Mass of Silicon] + [Mass of Oxygen]

  $$Mass = [2\times0.467(3.733\times10^{-7} A)] + [0.533(3.733\times10^{-7} A)] = \underline{\underline{5.477\times10^{-7}\ \text{A g}}}$$

- Thus the maximum thickness of the SiO film (area being constrained) can be found:

$$v_{SiO} = x_{SiO,Max} A = \frac{m_{SiO}}{\rho_{SiO}}$$

$$v_{SiO} = x_{SiO,Max} A = \frac{(5.477\times10^{-7} A)}{2.18}$$

$$\underline{\underline{x_{SiO,Max} = 2.512\times10^{-7}\text{cm} = 25.12\ \text{Angstroms}}}$$

- *Thus the maximum possible thickness of the oxide corresponds to an increase of 8.12Å, or 47.76 %.*
- This is likely to be an overestimate of the oxide thickness at the end of the mission, as the kinetics of the interfacial reactions to form SiO at 165°C are likely to proceed at a rate far slower than that which would allow complete conversion of SiO_2 to SiO in the timescale of the mission. Although ignored in this simple calculation, the elastic stresses induced by the conversion of SiO_2 to SiO would eventually be of sufficient magnitude to affect the total amount of conversion. If there were an elastic constraint imposed by the substrate on the SiO film (due to the vicious flow mechanisms suggested in [14] and [4]), then the driving force for further conversion to SiO would be decreased. However, effects such as the 'ballistic growth' [4] in the thin regime are observed, and the strain effects are used to explain the reduction in oxide growth rate for films in the thick regime (thicknesses in excess of ~30Å) [5, 14].

4.6 Relation of Suboxide Thickness to Total Oxide Thickness

The suboxide thickness is labelled δ in *Fig 4.1*. The total oxide thickness at any given time is the thickness of the suboxide plus the remaining thickness of the SiO_2 which has not yet been transformed into SiO.

As the suboxide grows, the SiO_2/SiO interface moves in the negative x-direction, and the SiO/Si interface moves in the positive x-direction (see *Fig. 4.1*). The important consideration when relating the total oxide thickness to the thickness of the growing suboxide layer is the difference between the densities of the SiO_2 and the bulk Si and the density of the product phase SiO. Both transformations involve a reduction in density (ρ_{Si} = 2.33 g cm^{-3}, ρ_{SiO2} = 2.196 g cm^{-3}, ρ_{SiO} = 2.18 g cm^{-3}) when the parent phases form SiO. Hence there is an overall increase in the thickness of the oxide layer (area constrained) as the lower density SiO is formed at the expense of its high-density parent phases. It is simple to see that the change in volume associated with the transformation of a unit volume of Si or SiO_2 into SiO is equal to the ratio of the density of SiO to

that of each phase. Thus for each cm^3 of Si transformed, 1.069 cm^3 of SiO is formed. Similarly 1.007 cm^3 of SiO is formed from 1 cm^3 SiO_2. This shows that as the SiO forms the two interfaces move at different relative velocities. The velocity of the interfaces is also controlled by kinetic factors such as rate of interfacial reaction and the rate of diffusion of oxygen and silicon within the system.

Although the above is an interesting observation, not enough is known about the velocities of the interfaces, and a different approach must be taken to relate suboxide thickness to the total oxide thickness. This approach is similar in concept to that used to calculate the maximum suboxide thickness in the previous section. In order to show the relation between suboxide thickness and total oxide thickness, it is necessary to calculate the thickness of the suboxide that may be formed when 90%, 80%, 20%, etc. of the SiO_2 is transformed to SiO. This is directly proportional to the number of oxygen molecules released in the $SiO_2 \rightarrow SiO + O$ reaction. This is in turn proportional to the mass of Si that will be removed from the bulk Si in order to bond with the O released from the SiO_2.

- The first step is to calculate for each fraction of the initial mass of SiO_2 that is converted to SiO, the mass of the Si present in the system, and its distribution between the SiO_2 and the SiO. Selected results are presented in *Table 4.2*.

Mass of Si Initially Present (g) = 1.148E-05			
Fraction of Conversion SiO_2 to SiO	**New Mass Si (g)**	**Mass of Si in Remaining SiO_2 (g)**	**Mass of Si in SiO (g)**
1	2.296E-05	0.000E+00	2.296E-05
0.5	1.722E-05	8.610E-06	8.610E-06
0.25	1.435E-05	1.076E-05	3.588E-06
0.1	1.263E-05	1.137E-05	1.263E-06
0	1.148E-05	1.148E-05	0.000E+00

Table 4.2: Distribution of Si as suboxide grows

- The next step is to calculate the distribution of oxygen in the system as a function of the fraction of SiO_2 transformed – *Table 4.3*.

Mass of O Initially Present (g) = 1.31E-05		
Fraction of Conversion SiO_2 to SiO	**Mass of O in Remaining SiO_2 (g)**	**Mass of O in SiO (g)**
1	0.000E+00	1.310E-05
0.5	6.550E-06	6.550E-06
0.25	9.825E-06	3.275E-06
0.1	1.179E-05	1.310E-06
0	1.310E-05	0.000E+00

Table 4.3: Distribution of O as suboxide grows

- From Tables 4.2 and 4.3, the mass of the SiO and the remaining SiO_2 films for each fraction of conversion may be calculated.
- Once the mass of the film at any given fraction of conversion is known, the volume and hence the thickness (area constrained) of each film may be found in a similar way to finding the maximum thickness of the SiO layer from knowing its mass in the previous section. *Table 4.4* shows the results of these calculations.

Fraction of Conversion SiO_2 to SiO	Thickness of SiO film (Å)	Thickness of remaining SiO_2 (Å)	Total Oxide Thickness (Å)
1	25.12	0.00	25.12
0.5	10.56	8.50	19.06
0.25	4.78	12.75	17.53
0.1	1.79	15.30	17.09
0	0.00	17.00	17.00

Table 4.4: Relation of thickness of SiO and SiO_2 films to total oxide thickness.

- *Fig 4.4* shows graphically how the total oxide thickness varies with the thickness of the SiO layer.

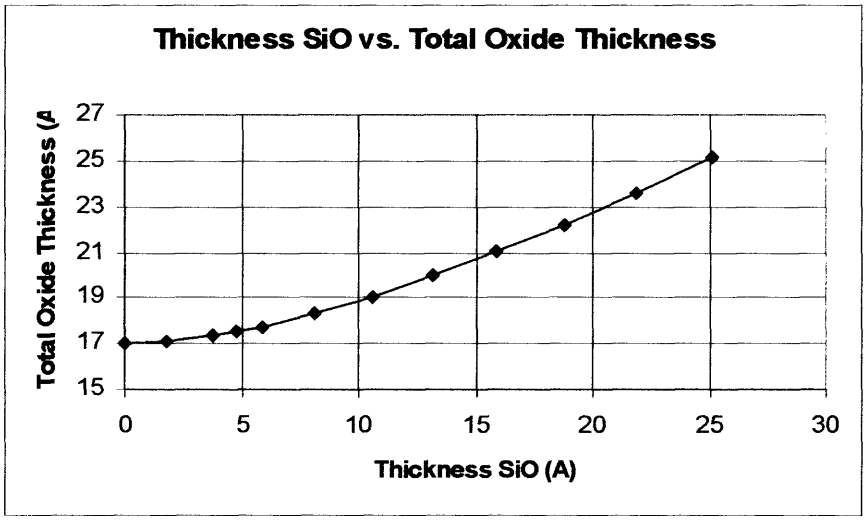

Fig 4.4: Relation of thickness of SiO film to total oxide thickness.

- This graph allows the prediction of a kinetic model (the thickness of the SiO layer) to be translated into a value for the total thickness of the oxide layer present on the surface of the Si substrate. The non-linearity of the plot is a result of the different density values across each of the interfaces, i.e. $(\rho_{Si} - \rho_{SiO}) \neq (\rho_{SiO_2} - \rho_{SiO})$.

The previous two sections have employed simple volume-conversion calculations to predict a maximum possible suboxide (and by definition total oxide) thickness of *25.12 Å*. *Fig 4.5* allows conversion of the predicted suboxide thickness to that of the total oxide present on the surface of the collector plates, and predicts a non-linear relation between total oxide thickness and suboxide thickness. It is hoped that with further experimentation, the kinetic models and *Fig 4.5* may soon be used to provide a more accurate prediction of thermally grown oxide thickness. The maximum thickness result may be used as a good first approximation to assess the extent of thermal oxidation of the collector arrays as opposed to oxidation caused by radiation effects, etc., as set out at the beginning of this chapter.

5.0 Summary and Conclusions

The goals of this study were two-fold:

1. *The clean subdivision of the collector materials once they were returned to Earth.*
2. *The development of a kinetic model to characterize and predict the thickness of the oxide layer on the returned collector arrays.*

The first goal involved a great deal of experimentation, while the second involved several in-depth derivations. This section comprises a brief summary of the results obtained.

- The subdivision of Si collector materials was investigated using a New Wave Research AccuScribe laser scribing system. Experimentation yielded the following results:
    i. Scribe width was found to be independent of the speed of scribing. However, the slower the scribing speed, the greater the amount of material that was removed from the scribe path. It was concluded that slower scribing speeds produce deeper scribes as the scribe width remained constant. However, slower scribing speeds increase the amount of heat seen by the material surrounding the scribe path. An optimum balance between the speed of scribe and the minimisation of heating of the sample has yet to be found.
    ii. Scribe width was found to be independent of the depth increase per pass. The greatest amount of material was removed for a depth increase of per pass of 5 μm/pass. The ejection of this debris was found to be somewhat fortuitous in that the debris was of sufficient quantity and size to shield the surface of the silicon surrounding the scribe path from the heating effects of the unfocused laser beam. This effect was optimised at a 5 μm/pass increase.
    iii. Several procedures for the identification of the planes of symmetry in the silicon wafers were attempted. Unfortunately reliable identification of said planes was not achieved with the published procedures [36, 37].
    iv. The three-point-bend testing proposed to quantify 'success' when altering scribing parameters was shown to be a very promising method of analysis. However, the procedure has yet to be proven on a large experimental data set.
- A kinetic model to predict the growth of the oxide layer on the surface of silicon collector materials during the mission as a result of thermal effects was developed successfully, but its application proved problematic. The following results were obtained from the process:
    i. A diffusion-based growth model for the oxidation of the existing SiO_2 layer present pre-flight into a less dense SiO layer when exposed to an elevated temperature and in the vacuum of space was successfully developed. Growth rate expressions for the oxide layer thickness under the two limiting kinetic cases of diffusion- and reaction-control. The growth rate expressions obtained for these cases predict parabolic and linear growth of the oxide film with time respectively. The separation of growth rates depending on film thickness is in agreement with the concepts originally proposed by Deal and Grove [11] and many subsequent studies [4, 5, 13-18, 24-26]. Comparisons with the literature suggest that the growth of the film when its thickness is below 30Å would be governed by the parabolic growth law, and hence be diffusion-controlled.
    ii. Application of the diffusion-based growth model proved to be impossible at this time, as many experimentally determined constants remain unknown, and are not available in the literature.
    iii. A second model was derived in an effort to reduce the number of unknown variables. This model was developed in a similar fashion to a published model by Whidden et al. [6, 7] which explicitly identifies the formation of SiO as an

intermediate compound in the oxidation of Si to SiO_2. A growth rate law was derived from this for the Genesis conditions. However, although the number of unknown variables was reduced, some remain and the model still cannot be applied.

iv. In lieu of a readily applicable kinetic model, an upper bound for the oxide thickness that may be formed by conversion of the SiO_2 layer to a layer of less dense SiO may be calculated by simple volume conversion. It was found that the maximum thickness of the oxide layer due to thermal effects would be 25 Å, a 48 % increase in thickness over the SiO_2 layer present before flight. It is also acknowledged that the maximum thickness is unlikely to be achieved, as the elastic constraint imposed by the substrate on the SiO film (due to the vicious flow mechanisms suggested in [14] and [4]), reduces the driving force for further conversion to SiO. However, effects such as the 'ballistic growth' [4] in the thin regime are observed, and the strain effects are used to explain the reduction in oxide growth rate for films in the thick regime (thicknesses in excess of ~30Å) [5, 14]. It was also found that the relation between the growth of the suboxide layer SiO and the increase in total thickness was non-linear due to the fact that $(\rho_{Si} - \rho_{SiO}) \neq (\rho_{SiO_2} - \rho_{SiO})$. The relation between the suboxide thickness and the total thickness of the oxide layer on the silicon was calculated and plotted. The maximum thickness result may be used as a good first approximation to assess the extent of thermal oxidation of the collector arrays as opposed to oxidation caused by radiation effects, etc., as set out at the beginning of this chapter.

The events of September 8th greatly influenced the subject and extent of this research. Should the scribing of the collector materials become a priority in the future, further experimentation would include a quantitative analysis of the scribe depth as a function of both the scribing speed and the depth/pass, a full investigation as to the optimal number of passes, all of which would ideally be quantified by use of the three-point-bend test procedure. A reliable and reproducible method of identifying the crystallographic orientation of the collector wafers should also be developed. In order to make the kinetic models predictive, the unknown rate constants, concentrations and experimental fitting parameters must be found, using the experimental methods proposed in *Section 4.3*, and those used by Whidden et al. [6,7].

6.0 Bibliography

[1] Genesis Official Website, http://www.genesismission.org
[2] K. McNamara, private communication (2003).
[3] K. McNamara, private communication (1999).
[4] H. Z. Massoud, Solid-State Electronics (1997), 41(7), 929-934.
[5] H. Kageshima; K. Shiraishi, M. Uematsu., Japanese Journal of Applied Physics, Part 2: Letters (1999), **38**(9A/B), L971-L974.
[6] P. Thanikasalam, T. K. Whidden, D. K. Ferry, Journal of Vacuum Science & Technology, B: Microelectronics and Nanometer Structures (1996), **14**(4), 2840-2844.
[7] P. Thanikasalam, T. K. Whidden, D. K. Ferry, M. J. Rack, Journal of Vacuum Science & Technology, B: Microelectronics and Nanometer Structures (1995), **13**(4), 1618-25.
[8] K. Choi, H. Harris, S. Gangopadhyay, H. Temkin, Materials Research Society Symposium Proceedings (2003), **765**, 85-90
[9] M. Morita, T. Ohmi, E. Hasegaw, M. Kawakami, K. Suma, Applied Physics Letters (1989), **55**(6), 562-4.
[10] F. Li, M. K. Balazas, B. E. Deal, Solid State Technology (2000), **43**(2), 87-98
[11] B. E. Deal, A. S. Grove, Journal Applied Physics (1965), **36**, 3770.
[12] Massachusetts Institute of Technology, Class 6.774 (2004), Lect. 10, 12.
[13] C. J. Han, C. R. Helms, Proc. - Electrochemical Society (1987), 87-10 (Proc. Symp. Silicon Nitride Silicon Dioxide Thin Insul. Films, 2nd, 1986), 315-24.
[14] E. H. Nicollian, A. Reisman, Journal of Electronic Materials (1988), **17**(4), 263-72.
[15] E. A. Irene, H. Z. Massoud, E. Tierney, Journal of the Electrochemical Society (1986), **133**(6), 1253-6.
[16] H. Z. Massoud, J. D. Plummer, E. A. Irene, Journal of the Electrochemical Society (1985), **132**(11), 2685-2693.
[17] H. Z. Massoud, J. D. Plummer, E. A. Irene, Journal of the Electrochemical Society (1985), **132**(11), 2693-700.
[18] H. Z. Massoud, J. D. Plummer, E. A. Irene, Journal of the Electrochemical Society (1985), **132**(7), 1745-53.
[19] A. Ourmazd, D. W. Taylor, J. A. Rentschler, J. Bevk, Physical Review Letters (1987), **59**(2), 213-16.
[20] P. J. Grunthaner, M. H. Hecht, F. J. Grunthaner, N. M. Johnson, Journal of Applied Physics (1987), **61**(2), 629-38.
[21] F. J. Himpsel, F. R. McFeely, A. Taleb-Ibrahimi, J. A. Yarmoff, G. Hollinger, Physical Review B (Condensed Matter) (1988), **38**(9), 6084-96.
[22] T. Hattori, M. Muto, T. Suzuki, Editor(s): Chadi, James D.; Harrison, Walter A. Proc. Int. Conf. Phys. Semicond., 17th, Springer (1985), New York, NY, 229-32.
[23] S. I. Raider, Phys. Chem. SiO_2 Si-SiO_2 Interface, (Proc. Symp.) (1988), 35-42.
[24] E. F. da Silva Jr., E. A. de Vasconcelos, B. D. Stosic, Applied Surface Science (2002), **190**(1-4), 30-4.
[25] M. A. F. Gomes, E. F. da Silva Jr., J. Albino Aguiar, Semiconductor Science and Technology (1995), **10**(7), 1037-9.
[26] E. F. da Silva Jr., B. D. Stosic, Semiconductor Science and Technology (1997), **12**(8), 1038-45.
[27] Scentific Group Thermodata Europe: Phase Diagram Collection: Si-O, http://web.met.kth.se/dct/pd/
[28] LANL Genesis Data Site, http://genesis.lanl.gov
[29] R.W. Balluffi, S. M. Allen, W.C. Carter, *"Kinetics of Materials"*, John Wiley & Sons, New York (2005), 510-512.
[30] I. Barin, F. Sauert, E. Schultze-Rhonhof, W. Shu Sheng, *"Thermochemical Data of Pure Substances"*, Weinheim, Federal Republic of Germany; VCH, New York; (1993), 2nd Ed., 1334-5, 1358-60.

Bibliography

[31] L.B. Pankratz, R.V. Mrazek, *"Thermodynamic Properties of Elements and Oxides"*, U. S. Dept. of the Interior, Bureau of Mines (1982), 278, 382-3, 386-90.

[32] M. W. Chase Jr., *"NIST-JANF Thermochemical Tables"*, American Chemical Society, Wshington DC; American Institute of Physics for NIST (1998), 4th Ed., 1717, 1745, 1751-3.

[33] M. L. Yu, B. N. Eldridge, Physics Review Letters **58** (1987), 1691-94.

[34] E. A. Gulbransen, K. F. Andrew, F. A. Brassart, Journal of the Electrochemical Society (1966), **113**(8), 834-7.

[35] R. E. Reed-Hill, R. Abbaschian, *"Principles of Physical Metallurgy"*, PWS Publishing Co. (1994), 3rd Ed, 735-6.

[36] M. H. Jones, S. H. Jones, Virginia Semiconductor Inc. (2003), http://www.virginiasemi.com/pdf/siliconetchingandcleaning.pdf

[37] W. C. Dash, Metallurgical Society Conferences (Proc.) (1959), **5**, 195-208.

[38] American Society of Testing and Materials, Standard # ASTM C 1161 – 02c (2003).

[39] E. A. Lewis, E. Kobeda, E. A. Irene, Proc. of 5th International Symp. on Si Materials Science and Technology: Semiconductor Silicon (1986), 416-25.

[40] DoITPoMS Teaching and Learning Package: *"Observing Dislocations"*, © University of Cambridge, http://www.doitpoms.ac.uk/tlplib/dislocations/observing.php

[41] K. A. Bezjian, H. I. Smith, J. M. Carter, Journal of the Electrochemical Society (1982), **129**(8), 1848-50.

[42] T. Cleghorn, private communication (2005).